AIAA SciTech Forum
12-16 January 2026, Orlando, FL
AIAA SCITECH 2026 Forum

10.2514/6.2026-0939

Optimal Spatio-Temporal Pulsed Control for Two-Dimensional Airfoil Aerodynamics

Sergio A. Castiblanco-Ballesteros*
San Diego State University, San Diego, CA, 92182

A. Leonid Heide†
University of Minnesota, Minneapolis, MN, 55455

Maziar S. Hemati‡
University of Minnesota, Minneapolis, MN, 55455

Gustaaf B. Jacobs§
San Diego State University, San Diego, CA, 92182

A parametric study of the sensitivity of location and timing of a pulsed control on the aerodynamics of a NACA-65-412 airfoil at $Re = 2\times10^4$ is presented. A net-zero-mass Dirac delta pulse in time with spatial Gaussian distribution is independently placed at six locations between the leading edge and the fixed separation location at the zero, averaged skin friction point. The pulse is also independently applied at six time instances within one period of the baseline flow's limit cycle. Lagrangian flow field analysis shows that this control triggers Kelvin–Helmholtz instabilities in the separated shear layer. A continuous wavelet analysis of lift and velocity signals reveals that sub-cycle variations in pulse timing—at fixed spatial positions—can flip the flow from pronounced lift suppression to transient reattachment, achieving up to 30% lift enhancement. A time-frequency analysis shows that vortex interlocking between instability-driven vortices and naturally occurring counter-rotating structures near the trailing edge underpins these dramatic transitions.

I. Introduction

Flow separation can degrade performance in many engineering systems, through reduced lift, increased drag, and decreased efficiency. To alleviate the effects of flow separation on aerodynamic performance, flow control has been considered since the inception of the field of aerodynamics [1, 2] and continues to be one of the premier challenges in modern aerodynamics. While classic flow control concepts work by completely removing or re-energizing the separated fluid through suction and blowing (see e.g. Schlichting [3]), more recent techniques take advantage of instabilities and non-linearities in the flow by using more compact zero-net mass flux (ZNMF) devices [4]—such as plasma actuators [5–7], fluidic oscillators [8–12], and synthetic jets [13–21]. These have been shown to effectively alter separated flows, and in some cases to even yield complete reattachment.

To design an effective flow control strategy in boundary-layer dominated aerodynamics, as a first step, a fundamental understanding and flow separation physics and theory is necessary. The foundational work of Prandtl [22] established the basic concept of separation in steady flows, identifying separation points as locations of vanishing skin friction. Separation typically occurs when an adverse pressure gradient causes the near-wall flow to reverse, leading to the vanishing friction and resulting in flow detachment. For unsteady flows, criteria such as the Moore–Root–Sears framework [23–25] extended this notion by locating singularities in boundary-layer equations where the wall-normal velocity gradient, u_y, vanishes. Liu [26] later showed that such singularities do not arise in the full two-dimensional Navier–Stokes equations, underscoring the limitations of boundary-layer approximations for unsteady separation. The development of triple-deck theory by Sychev [27] improved the near-wall modeling of high-Reynolds-number separation but still relied on asymptotic assumptions. In parallel, purely kinematic analyses by Shariff et al. [28] and Yuster &

*Ph.D. Student, Aerospace Engineering, scastiblancoba7077@sdsu.edu
†Ph.D. Candidate, Aerospace Engineering and Mechanics, heide116@umn.edu
‡Associate Professor, Aerospace Engineering and Mechanics, mhemati@umn.edu
§Professor, Aerospace Engineering, gjacobs@sdsu.edu

Hackborn [29] revealed that classical invariant manifolds from dynamical systems theory are inadequate for identifying separation structures near walls, due to the degeneracy induced by the no-slip condition. To address these limitations, modern Lagrangian approaches have emerged, offering frame-invariant, particle-based descriptions of separation. Haller [30] proposed an exact theory for unsteady separation in two-dimensional flows, defining separation points as the intersection of non-degenerate hyperbolic manifolds with the wall in time-periodic flows. He showed that these manifolds are time-varying. The approximate seperatrics have a fixed origin at the averaged, zero skin-friction location in time-periodic flows. Serra et al. [31] further advanced this perspective by introducing the "backbone of separation", a material line of maximum curvature that connects to the wall at fixed spiking points, thereby offering a robust, geometry-based characterization of separation with direct relevance for its control.

In parallel to the advancements in unsteady flow separation theory and aerodynamics theory in general, improved flow control techniques have naturally developed for lifting surfaces. In particular, a temporal flow control using synthetic jets was first explored by Amitay et al. [13, 14] and later by Glezer [15], who demonstrated that periodic jet pulses deployed along the no-slip surface can effectively trigger shear-layer instabilities and promote flow reattachment on airfoils, leading to substantial improvements in lift-to-drag ratios. Oscillatory forcing has also been considered to improve control authority over separation. Actuation at domination frequencies in the shear layer [32–35] or the separation bubble [36] have been shown to be effective. Nonlinear unsteady flow interactions can result in lock-on effects that influence the optimal forcing frequency [37, 38]. This lock-in can be leveraged to identify candidate actuation frequencies objectively using operator-based and data-driven modal analysis techniques—such as linear stability analysis, resolvent analysis, and dynamic mode decomposition (DMD) [18, 34, 39–42]. Kamphuis et al. [43] showed that a pulsed control can increase the angle of the Lagrangian separation manifold in the flow over a NACA65-412 airfoil and yield up to a 40% lift enhancement, highlighting the sensitivity of the flow to precise manipulation of separation dynamics. In a complementary two-dimensional study, Bhattacharjee et al. [44] demonstrated that pulsed actuation upstream of the asymptotic separation point is particularly effective, providing a more targeted and energy-efficient control mechanism. These favorable actuation sites coincide with the spiking separation points identified by Serra et al. [31], which emerge upstream of the long-term separation location. Despite substantial advances in identifying geometrically optimal actuator sites—such as the spiking separation points of Serra et al. [31] and the upstream asymptotic locations highlighted by Bhattacharjee et al. [44]—the temporal dimension of actuation remains comparatively unexplored. Applying a pulse at the an optimal spatial location near walls is only half of the problem; the pulse must also be delivered at an appropriate phase of the natural vortex-shedding cycle to maximize receptivity.

In this paper, we investigate the spatio-temporal sensitivity of a control of separation over a cambered NACA 65(1)-412 airfoil at Re = 20,000 and an angle of attack of 4°. Building on Direct Numerical Simulations studies of the NACA65-412 aerodynamics [43, 45–47], we introduce zero-net-mass-flux Gaussian pulses at selected chordwise locations and at prescribed phases of the natural shedding cycle, we probe the wake's receptivity to spatially and temporally localized excitation following Bhattacharjee et al. [44]. We show how these pulses generate a transient Kelvin–Helmholtz instability in the separated shear layer, using finite-time Lyapunov exponents (FTLE) to identify the Lagrangian coherent structures (LCS) and to examine their interaction with the wake near the trailing edge. A total of 36 pulsed cases is analyzed, comprising six actuation locations and six activation times. Alongside lift and drag coefficients, we quantify asymptotic separation [30] and spiking [31] angles. By relating these measures to the presence and strength of the K–H response, we identify actuation settings that most effectively modify the aerodynamic loads, with the aim of informing flow-control strategies that exploit separation dynamics. In addition, we apply a continuous wavelet transform (CWT) to analyze the unsteady flow response in terms of a magnitude scalogram that reveals energy content as a function of time and frequency [48, 49]. The CWT is aplied to both global force signals and pointwise velocity traces, generating time–frequency scalograms that reveal narrow phase windows and specific spatial regions of maximal energy injection. To extend this analysis to the full velocity field without prohibitive cost, we apply the CWT on model responses obtained using the proper orthogonal decomposition (POD): specifically, POD extracts a common modal basis from all cases, then CWT is performed on the normalized temporal coefficients and the full scalogram is reconstructed—complete with intermodal cross-terms—by re-weighting each wavelet coefficient by its relative contribution to the total energy. This hybrid POD–CWT framework yields a global, directly comparable time–frequency map of the flow; uncovers the multi-scale coupling between high-frequency shear-layer instabilities and low-frequency wake dynamics; and demonstrates the extreme sensitivity of separated flows to small, phase-locked perturbations.

The paper is organized as follows. The methodology section presents the governing flow equations and numerical schemes, the DNS setup, and the formulation of the zero-net-mass Gaussian pulse, including actuation locations and activation times; it also details the computation of FTLE-based LCS and the diagnostics used to track the transient

K–H response. In the subsequent section, we develop the mechanism of K–H evolution and report the parametric study results, together with separation-angle measurements and the POD–CWT scalogram analysis. Finally, the conclusions section summarizes the main findings and outlines directions for future work.

II. Methodology and Methods

A. Governing Equations and Numerical Approximation

We consider the compressible Navier–Stokes equations for conservation of mass, momentum, and energy, written in non-dimensional form with the flux vector split into advective (superscript a) and viscous (superscript v) contributions:

$$\frac{\partial \mathbf{Q}}{\partial t} + \mathbf{F}_x^a + \mathbf{G}_y^a - \frac{1}{Re_f}\left(\mathbf{F}_x^v + \mathbf{G}_y^v\right) = \mathbf{S}, \tag{1}$$

where the solution vector is $\mathbf{Q} = [\,\rho \quad \rho u \quad \rho v \quad \rho E\,]^T$, and ρ, u, v, and E denote density, the velocity components in x- and y-direction, and the total energy, respectively. The equation of state closes the system, $p = \frac{\rho T}{\gamma M_f^2}$. All quantities are non-dimensionalized with respect to a characteristic length scale, reference velocity, density, and temperature, yielding the non-dimensional Reynolds number Re_f and Mach number M_f.

The system (1) is spatially discretized using a discontinuous Galerkin spectral element method (DGSEM) and advanced in time with a fourth-order explicit Runge–Kutta scheme. Gauss–Lobatto quadrature nodes are employed for the spatial integration, and a kinetic-energy-conserving split-form approximation of the advective volume fluxes ensures stability of the scheme through cancellation of aliasing errors associated with the nonlinear terms. For a detailed description of the numerical scheme and the setup for airfoil simulations we refer to Klose *et al.* [50].

B. Lagrangian flow separation metrics

The theory of fixed Lagrangian flow separation as proposed by Haller [30], defines a separation line as the manifold that attracts fluid parcels from material lines that are initially parallel to the wall (as illustrated in figure 1). This Lagrangian separation manifold has a fixed origin, γ, and the angle of the manifold with respect to the wall tangent at this origin is varying over time, $\alpha(t)$. The origin of separation is determined by integrating the skin-friction field along the wall and in its vicinity. Zeros of the time averaged tangential skin-friction coefficient, c_f, identify the origin's location. The separation angle is determined through an asymptotic time integration of the friction of the skin and the gradients of the wall pressure [30]. For short (non-asympotic) times, Serra et al. [31] showed that the material lines well up upstream of this asymptotic line. This upwelling phenomenon was coined as spiking, and is identified by the maxima of the curvature evolution of initially wall-parallel lines (gray lines in figure 1). The wall-intersection of this backbone defines the "birth of flow separation", or spiking point s. The associated spiking angle, $\beta(t)$, as schematically illustrated in figure 1 is varying over time and can be determined with finite integration of the wall based flow velocity gradient [31]. Both the responses of asymptotic separation angle and spiking angles to a pulsed actuation are measured to understand the effect of flow control on these Lagrangian flow separation metrics. Figure 1 shows that ridges in the finite time Lyapunov exponent (FTLE) field determined in backward time, intersect with the separation line and confine the upwelling region. The backward-time FTLE ridge is an attractor and a near zero-mass flux line that connects the separation line, with larger coherent structures downstream of the separation area [46].

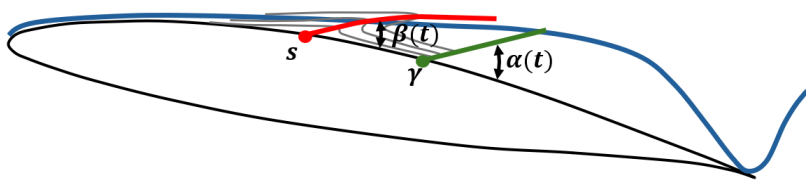

Fig. 1 Schematic definition of the asymptotic separation (green) angle $\alpha(t)$ and the spiking (backbone in red) angle $\beta(t)$ at a representative suction-side wall point. The asymptotic separation line is obtained from Haller's exact separation theory [30], while the backbone of separation follows Serra *et al.* [31]. Both angles are measured between the corresponding material line and the local wall-tangent direction.

C. DNS of Pulsed Flow over Airfoil

The flow over a NACA 65(1)-412 airfoil is simulated at a Reynolds number based on the chord length of $Re_c = 20{,}000$, a Mach number of $M = 0.3$, and an angle of attack of 4°. The low Mach number ensures a nominally incompressible flow. The computational domain, shown in figure 2, consists of 2,256 quadrilateral elements. The domain dimensions are chosen to prevent blockage and follow the recommendations of Nelson *et al.* [45]. The wall-boundary elements are curved and fitted to a spline representation of the airfoil surface, again following Nelson *et al.* [45]. Boundary conditions are imposed weakly on the fluxes using a Riemann solver [51]. The solution vector is approximated with a 12^{th}-order polynomial, giving a total of 381,264 collocation points in the domain. Lagrangian particles are initialized in the airfoil-neighboring elements to compute flow maps and FTLE fields [46, 52].

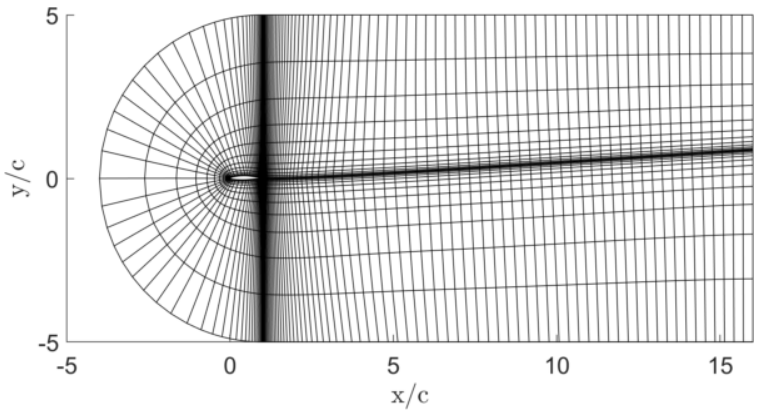

Fig. 2 Two-dimensional computational domain for the NACA 65(1)-412 airfoil. Only elements without interior Gauss–Lobatto nodes are shown.

A source term, $\mathbf{S}(t, \mathbf{x})$, in (1) models the pulsed actuation following the formulation described in Kamphuis *et al.*,

$$\boldsymbol{S}(t,\boldsymbol{x}) = \boldsymbol{b}(t) \odot \frac{\boldsymbol{a}}{\sqrt{(2\pi)^n \left|\boldsymbol{\Sigma}^{-1}\right|}} \exp\left[-\frac{1}{2}(\boldsymbol{x}-\boldsymbol{c})^T \boldsymbol{\Sigma}^T (\boldsymbol{x}-\boldsymbol{c})\right], \tag{2}$$

where $\odot$ denotes the Hadamard product, $\boldsymbol{\Sigma}$ is the covariance matrix of dimensions $n \times n = 2 \times 2$, $\boldsymbol{a}$ is the vector of amplitudes, and $\boldsymbol{c}$ identifies the center coordinates of the Gaussian distribution. We set $\boldsymbol{\Sigma}$ to

$$\boldsymbol{\Sigma} = \begin{bmatrix} \frac{\cos^2\theta}{2\sigma_x^2} + \frac{\sin^2\theta}{2\sigma_y^2} & \frac{\sin 2\theta}{4\sigma_x^2} - \frac{\sin 2\theta}{4\sigma_y^2} \\ \frac{\sin 2\theta}{4\sigma_x^2} - \frac{\sin 2\theta}{4\sigma_y^2} & \frac{\sin^2\theta}{2\sigma_x^2} + \frac{\cos^2\theta}{2\sigma_y^2} \end{bmatrix}, \tag{3}$$

for $\theta \in [-45°, 45°]$, so that the principal axes of the Gaussian function are rotated by an angle θ with respect to the y-axis. The variances are given by

$$\sigma_x = 0.0012/\sqrt{2} \quad ; \quad \sigma_y = 0.0096/\sqrt{2}. \tag{4}$$

The vector of amplitudes, $\boldsymbol{a}$, is specified as

$$\boldsymbol{a}(t) = \left[0 \ , \ \sqrt{(2\pi)^n \left|\Sigma_{mj}^{-1}\right|} \ , \ \sqrt{(2\pi)^n \left|\Sigma_{mj}^{-1}\right|} \ , \ \sqrt{(2\pi)^n \left|\Sigma_{mj}^{-1}\right|}\right], \tag{5}$$

and the time-dependent component, $\boldsymbol{b}$, is given by

$$\boldsymbol{b}(t) = \delta(t-T)\,[0, \ -\sin(\theta), \ \cos(\theta), \ u(x,t)b_2(t) + v(x,t)b_3(t)]^T, \tag{6}$$

where $\delta(\tau)$ is the Dirac delta function. The source is zero-mass, and the angle θ is chosen such that the principal axis of the Gaussian function is approximately normal to the airfoil surface. The Dirac delta conveniently integrates in time to

the Heaviside function, so that numerically the pulse is implemented by superposing a Gaussian distribution onto the solution vector at time T.

The data required as input for the analysis of the optimal location and timing of pulsed control are obtained by conducting DNS and systematically sampling the parameter space spanned by $\boldsymbol{c}$ and T. Table 1 collates the values for which simulations are performed. The source center $\boldsymbol{c}$ in equation (2) is located at a distance of $2\sigma_y$ into the flow, measured normal to the airfoil suction side, at the chordwise locations listed in the table (following [53]). Activation times are expressed as sixths of the natural period of the lift. Combinations of all locations and activation times yield a total of 36 test points. Figure 10 shows the activation times with respect to the phase of the lift coefficient.

x/c	0.1	0.2	0.3	0.4	0.45	0.5
T	$0(T_f/6)$	$1(T_f/6)$	$2(T_f/6)$	$3(T_f/6)$	$4(T_f/6)$	$5(T_f/6)$

Table 1 Locations, x/c, on the suction side of the airfoil for the source actuation, and corresponding activation times, T, expressed as fractions of the base-flow natural period T_f.

III. Results and Discussion

A. Flow Physics

As a reference to the systematic investigation of the optimal spatio-temporal pulsed flow control, we first discuss the baseline flow field. Figure 3 visualizes forward and backward FTLE fields at $t = 0.8$, immediately preceding the pulse activations of figure 8. The asymptotic separation point is located at $x/c = 0.5$ on the suction side of the airfoil. The dashed red curve indicates the time-averaged asymptotic separation line following the framework of Haller [30], which aligns downstream with the FTLE ridge marking the separation shear layer. The spiking point for this flow, following Serra et al [31] is located at $x/c = 0.45$. Downstream of the separation point the flow remains fully separated, forming an open recirculation region. The FTLE fields reveal not only the separation manifold but also the onset of wake-shedding structures at the trailing edge, as well as the material barriers and transport pathways that organize vortex formation and convection.

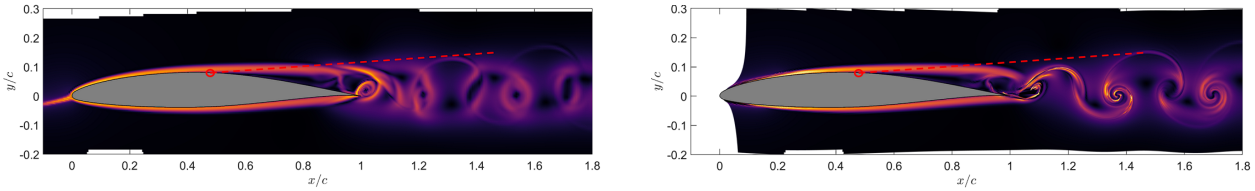

(a) Forward FTLE. **(b) Backward FTLE.**

Fig. 3 Baseline forward and backward FTLE fields at time $t = 0.8$, right before pulse activations shown in Figure 8. The dashed red line shows the average asymptotic separation line. The shear layer $(x_{\mathrm{sh}}(s), y_{\mathrm{sh}}(s))$ is identified as the positive ridge of the time-averaged forward FTLE.

Figure 4 shows the post-actuation evolution for $x/c = 0.45$ with activation time $t_p = 2(T_f/6)$. The ridges in the forward-time FTLE field repel fluid. The openings on the FTLE ridge can be interpreted as a local loss of barrier function and material entrainment at the shear-layer interface [54]. The distance between openings are directly connected to the fastest growing modes of the Kelvin-Helmholtz instabilities, as discussed in [55]. In panel (a) ($t - t_p = 0.36$), three Kelvin–Helmholtz vortices, that are also called packets, numbered one to three from downstream to upstream, emerge along the separated shear layer. They increase in strength as they are advected downstream. By panel (b) ($t - t_p = 0.8$), these vortices have grown and the ridge openings have widened, signaling enhanced entrainment of the outer flow's momentum into the separated region. At this time, vortex 1 is interacting with the counter-clockwise vortex generated on the pressure side at the trailing edge; the two structures interlock and are subsequently shed into the wake. At $t - t_p = 1.54$ (panel (c)), an interlocking surface R forms between the vortex 1 that has shed off and vortex 2. This surface modifies the local circulation and persists long enough to trap the counter-clockwise trailing-edge

vortex between R and the suction surface, producing a net downward impulse and a marked reduction in lift—consistent with the drop observed in figure 8. Panel (d) ($t - t_p = 2.0$) shows R spanning the trailing-edge region and temporarily suppressing trailing-edge vortex formation, while vortices 3 and 4 continue to sustain openings in the FTLE ridge, thereby preserving the entrainment into the separated region. As the packet decays (panel (e), $t - t_p = 2.74$), the wake reorganizes toward the baseline configuration; by panel (f) ($t - t_p = 3.68$), the flow closely resembles the unforced state.

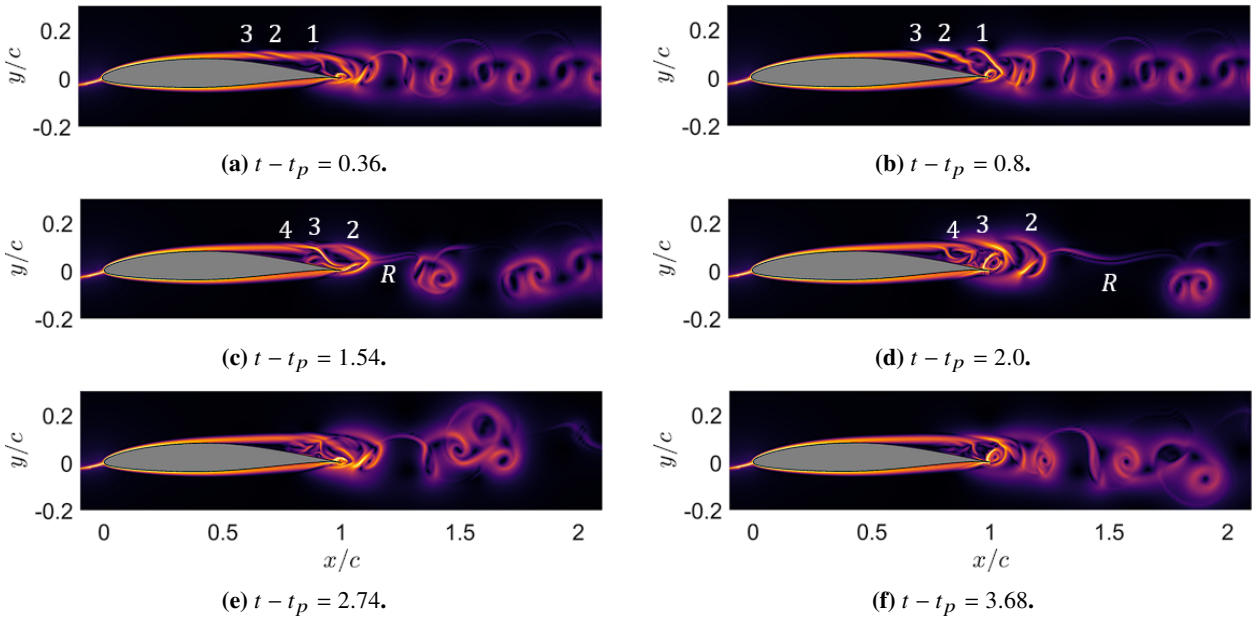

(a) $t - t_p = 0.36$. **(b)** $t - t_p = 0.8$.

(c) $t - t_p = 1.54$. **(d)** $t - t_p = 2.0$.

(e) $t - t_p = 2.74$. **(f)** $t - t_p = 3.68$.

Fig. 4 Forward-FTLE time sequence illustrating the transient Kelvin–Helmholtz (K–H) response for a pulse applied at $x/c = 0.45$ and activated at $t_p = 2(T_f/6)$ (cf. red trace in Figure 8). Panels (a)–(f) show the formation and convection of a K–H wave packet that generates vortices labeled 1–4 and an interlocking (reattachment) material surface R. When R aligns with the trailing edge, lift increases; when R is displaced downstream (as in this case), the counter-clockwise vortex near the suction surface induces a downward impulse and lift decreases.

The evolution of the K–H instability and its effect on the wake as described here, is summarized in the schematic in figure 5, where time is normalized by the natural shedding period of the baseline flow, T. Red and blue lines denote positive and negative vorticity ridges in the wake, respectively, while dashed blue lines trace the development of K–H vortices. The orange line represents the instantaneous separation manifold, computed using both Haller's separation theory [30] and Serra's spiking theory [31].

The interlocking surface appears in all pulsed cases; the magnitude and sign of the lift response depend on its phase and location relative to the trailing edge. If R is displaced upstream or above the trailing edge (figure 4), the counter-clockwise vortex formed on the pressure side is trapped near the suction surface, imparting a downward momentum impulse on the suction side of the airfoil and thus reducing lift. In contrast, if R aligns with the trailing edge then transient reattachment is promoted, which prevents the counter-clockwise vortex from impinging on the suction side, and leads to a peak lift increase of about 30%. Clearly, the timing and placement of the pulse govern whether vortex interactions suppress or enhance aerodynamic performance.

Figure 6 comprises and compares the time-dependent responses to the pulsed actuation of several flow field variables, including the time-dependent response of (1) skin friction and (2) FTLE field on the suction side of the airfoil, (3) lift coefficient, and (4) the Lagrangian separation metrics. In the *skin-friction* panel, the pre-actuation field displays weak, upstream-leaning streaks indicative of a trailing-edge feedback on separation. Shortly after the pulse (black circle), a family of positively sloped c_f ridges emerges and convects downstream, the canonical signature of a K–H wave packet forming on the separated shear layer. Between $t \approx 3$ and $t \approx 5$ a strong, nearly vertical positive ridge appears, coincident with an increase in drag; this feature reflects the transient interruption of recirculation by the interlocking (reattachment) surface described earlier. The *forward-FTLE* panel shows the same event sampled along the shear-layer centerline (defined from the baseline), providing a Lagrangian view of the packet: the post-pulse growth of FTLE amplitude and the widening of ridge openings document material entrainment across the interface as the packet amplifies and travels

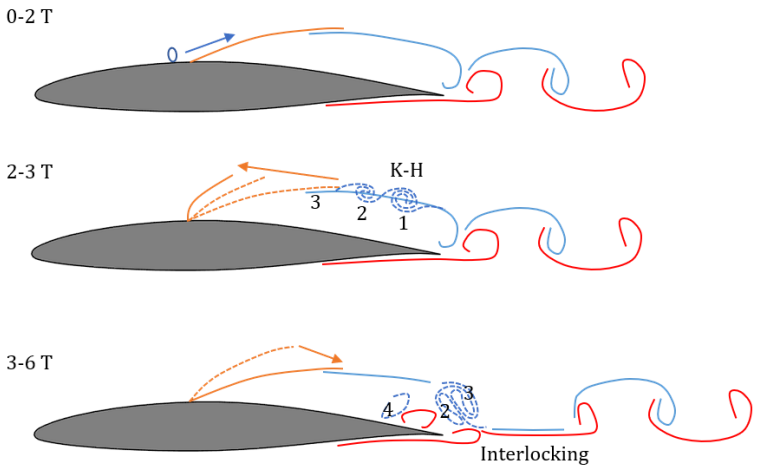

Fig. 5 Schematic of induced Kelvin–Helmholtz instability evolution. Continuous red and blue lines show the positive and negative vorticity ridges, respectively. Dashed blue lines show the instability evolution. The continuous blue line marks the zero-mass pulse location. The orange line denotes the separation manifold.

downstream. In the *forces* panel, the pulsed case (solid) departs from the baseline (dashed) with a sharp lift reduction and drag increase if and when the interlocking surface spans the trailing-edge region. This timing coincides with the FTLE having its largest magnitude (an thus attraction of fluid) and skin-friction signatures of the packet and the onset of vortex interlocking at the trailing edge. Finally, the *angles* panel tracks the instantaneous Lagrangian separation metrics. Both the asymptotic separation angle α and the spiking angle β increase following the packet onset and peak when the instability-generated vortices reach the trailing edge and reattachment is suppressed. The peak in β aligns with the lift minimum, highlighting the tight coupling between near-wall separation dynamics and global loads. Taken together, these panels demonstrate a clear causal chain: pulse $\rightarrow$ K–H packet growth and entrainment $\rightarrow$ formation of the interlocking surface near the trailing edge $\rightarrow$ transient load modification.

To quantify how the pulse modifies the shear layer, we first extract the forward-FTLE ridge that delineates the separated interface in the baseline field and parametrize it by arclength, $s \mapsto (x_{\mathrm{sh}}(s), y_{\mathrm{sh}}(s))$. Evaluating the FTLE on this material line over time yields space–time maps $\mathrm{FTLE}(x_{\mathrm{sh}}, t)$, shown in figure 7. The baseline panel 7a exhibits the familiar shedding at the trailing edge ($x/c = 1$) as an alternating banded pattern and a weak upstream-leaning trace (slope ≈ -0.36), indicative of wake feedback on the region of flow separation. In the actuated cases 7b–7d, the pulse instantaneously creates gaps (dark troughs) in the FTLE ridge—openings of the transport barrier—followed by a sequence of positively sloped bands that track the convecting K–H packet. Four prominent bands are visible, corresponding to the four vortices labeled previously: the first two disrupt and "lock" the flow near the trailing edge, while the latter two re-energize the recirculation zone as the packet decays. The case $x/c = 0.45$, $T = 2(T_f/6)$ has the most notable increase in drag and separation angles (see figure 21); figure 7b shows the forward FTLE extracted for this case, with the strongest and most persistent signature (lasting up to $t \approx 5$), which highlights the role of timing in aerodynamic performance.

For comparison, keeping the location fixed but delaying the activation to $T = 5(T_f/6)$ (figure 7c) substantially weakens the packet, again pointing to phase sensitivity. When the pulse is moved upstream to $x/c = 0.20$ (figure 7d), the K–H bands originate at the actuation site but steepen as they pass the spiking location at $x/c \approx 0.45$, after which their imprint is amplified—consistent with perturbation at that location having the most amplification in the shear layer and wake. For these particular cases, the black lines demarcate the lower edge of the bands generated by the pulse. There is a clear change in the slope of the perturbation as it evolves downstream around $x/c = 0.45$, indicating a change in advection velocity (u_a) from about $u_{a,1} = 0.65$ upstream of $x/c = 0.45$ to $u_{a,2} = 0.45$ downstream of $x/c = 0.45$. The downstream advection velocity remains essentially the same across all cases. To further address the question of optimal phase and location, we next perform a frequency-based analysis of the convective onset of instabilities using the combined POD–CWT framework.

A comparison of the temporal trends of the lift coefficient, c_l, and drag coefficient, c_d, between the baseline flow and the controlled flow with a pulsed actuation with a fixed spatial location at $x/c = 0.45$ and a varying time in Figure 8 shows that the flow requires approximately two shedding periods to exhibit a significant aerodynamic response

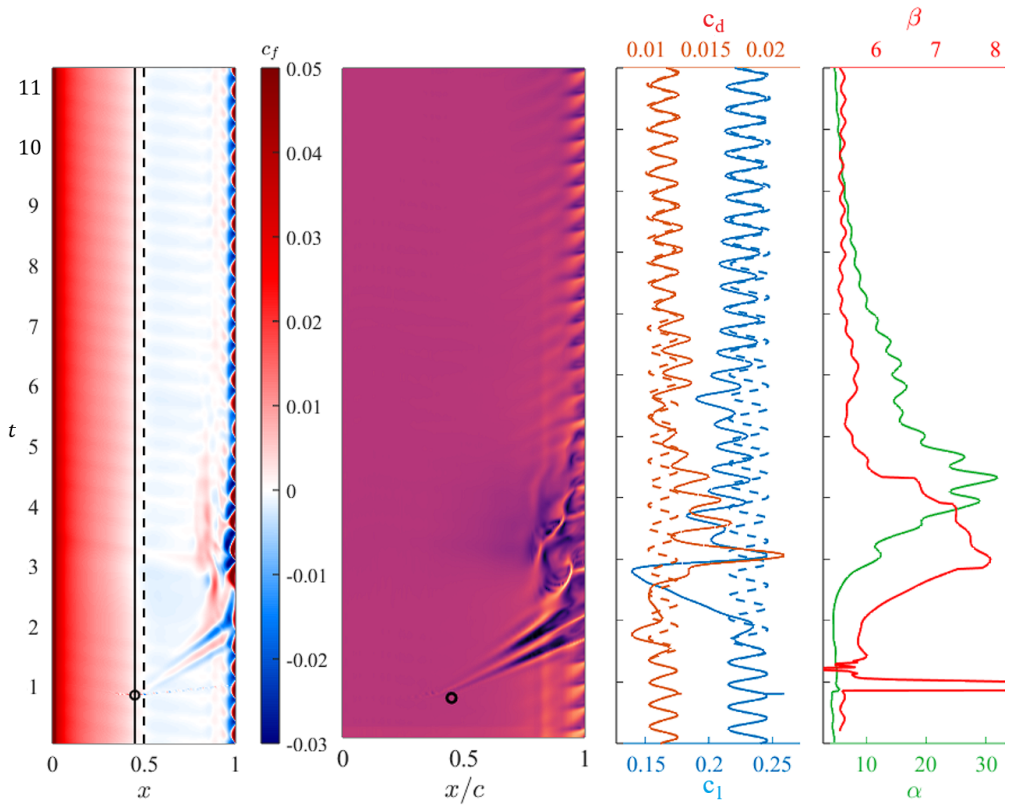

Fig. 6 Space–time diagnostics for the pulsed case at $x/c = 0.45$ with activation time $t_p = 2(T_f/6)$ (continuous red line in Figure 8). From left to right: (i) suction-side skin-friction coefficient $c_f(x,t)$; the dashed black curve marks the asymptotic separation point [30] and the solid black curve the spiking point [31]; the black circle marks the actuation location/time. (ii) Forward FTLE sampled along the separated shear-layer centerline, showing the convecting packet triggered by the pulse. (iii) Lift coefficient, c_l (blue) and drag coefficieint, c_d, (red): solid, pulsed; dashed, baseline. (iv) Asymptotic separation angle α (green) and spiking angle β (red), in degrees.

following actuation. This delay corresponds to the time needed for a Kelvin–Helmholtz (K–H) instability to develop fully within the separated shear layer as illustrated by a sequence of snapshots of the FTLE contours in Figure 4. The most pronounced response is observed for $T = 2(T_f/6)$, where a sharp drop in lift occurs between $t = 2$ and $t = 2.8$, reaching a maximum reduction of approximately 35% before recovering. Concurrently, the drag coefficient increases by nearly 40%. In contrast, pulses triggered at later times $T = 3(T_f/6)$ and $T = 4(T_f/6)$ result in favorable aerodynamic modifications, with lift increasing up to 15% above the baseline and a corresponding drag reduction of similar magnitude. These effects persist for 2–3 advective time units, demonstrating the lasting impact of a short-duration control input. The comparison underscores the critical role of actuation timing: even when applied at the same spatial location, variations in pulse timing can lead to markedly different aerodynamic outcomes, motivating predictive reduced-order models capable of capturing the unsteady physics underlying these transitions.

B. Time-Frequency Analysis of Lift Response

For each pulse location above the suction surface, we administered six pulses timed at equally spaced phases of the baseline vortex-shedding cycle (Figure 9). The resulting lift coefficient $c_l(t)$ was recorded after each pulse. As illustrated in figure 10, the lift response does not start at the exact time of the pulse application: each pulse must convect downstream and interact with the separation bubble before a transient lift response is observed.

In figure 10 (a) This delay is plotted against the activation time (phase in the shedding cycle), averaged over all actuator locations. For every phase the flow requires roughly two shedding periods to respond, with only a mild dependence on the activation time: the delay varies between about 1.7 and 2.1 cycles and is largest when the pulse is applied at $T = 3T_f/6$. This indicates that, regardless of when in the cycle the pulse is introduced, the Kelvin–Helmholtz

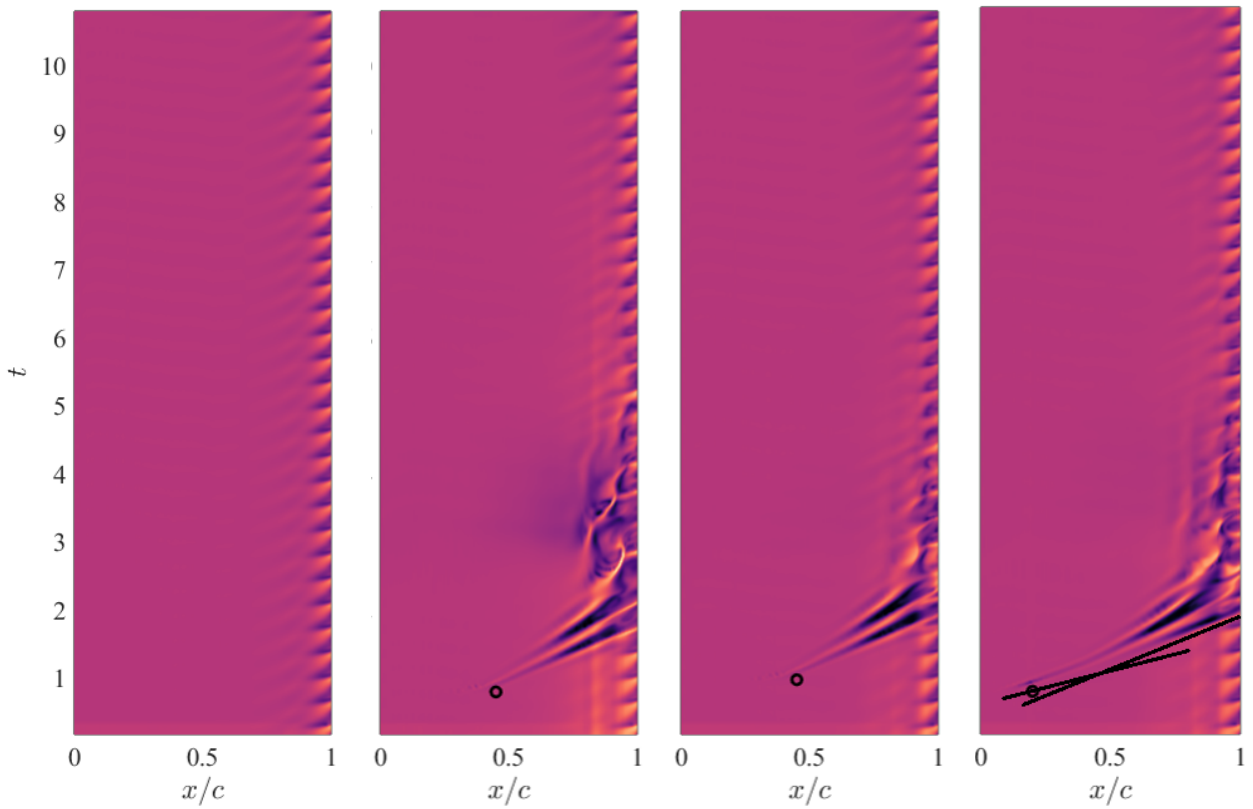

(a) Baseline. **(b)** $x/c = 0.45, T = 2(T_f/6)$**.** **(c)** $x/c = 0.45, T = 5(T_f/6)$**.** **(d)** $x/c = 0.20, T = 2(T_f/6)$**.**

Fig. 7 Forward FTLE, $\mathrm{FTLE}(x_{\mathrm{sh}}, t)$**, sampled along the separated shear-layer centerline for the baseline and three actuated cases. Two comparisons are shown: (i) fixed location (**$x/c = 0.45$**) with two activation times [**$T = 2(T_f/6), T = 5(T_f/6)$**], and (ii) fixed activation time [**$T = 2(T_f/6)$**] with two locations (**$x/c = 0.45, x/c = 0.20$**). Black circles mark the actuation location and time. Note that for the** $x/c = 0.20$ **case, there is a change in the average slope of the instability development.**

packet it generates must grow and convect to the trailing edge before it can significantly modify the global forces. In figure 10(b) the same delay is shown as a function of actuation location x/c, now averaged over all activation times. Here the dependence is much stronger and approximately monotonic: forcing near the leading edge ($x/c = 0.1$) produces the longest delay, close to three oscillations, whereas pulses near the trailing edge ($x/c = 0.6$) trigger a response after only about one cycle. The sharp decrease between $x/c = 0.40$ and $x/c = 0.45$ coincides with the separation region, highlighting it as a dynamically special zone where perturbations couple more rapidly into the global shedding dynamics.

Examining the raw $L(t)$ data reveals that only certain phase–location combinations produce appreciable changes in amplitude. To uncover the underlying spectral dynamics, we compute the CWT (convolutional wavelet transofrmation) of each lift trace and plot the magnitude scalogram $|W_x| = |W_L|$ for several perturbation timings at a pulse location of $x/c = 0.10$ in figure 12 and pulse location $x/c = 0.45$ in figure 13. In cases with weak lift modulation, the scalogram is dominated by the baseline shedding band, with no low-frequency content. By contrast, the high-response cases exhibit a pronounced broadband signal, reflecting the growth and decay of the transient separation-bubble oscillation [48, 49]. Note that the responses from pulsing at $x/c = 0.10$ are significantly weaker compared to the $x/c = 0.45$ cases. This is not surprising, as the perturbation needs more time to advect downstream, and is damped in the process.

These observations confirm that the appearance of a low-frequency band in the lift-coefficient scalogram correlates directly with strong transient wakes and altered mean loading. However, to rule out artifacts arising solely in the global force signal, we must verify whether the same low-frequency energy surge appears in pointwise FTLE measurements. This motivates the analysis presented in the next section.

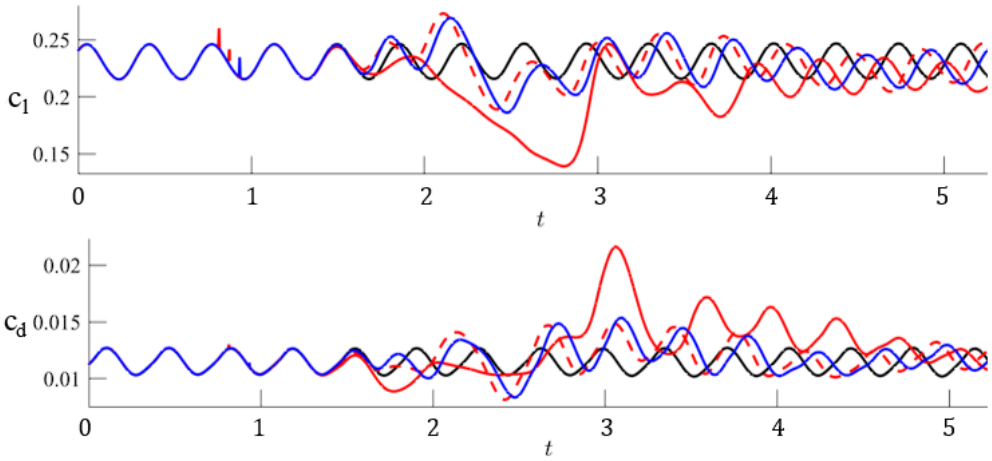

Fig. 8 Lift and drag coefficients for the same pulse location ($x/c = 0.45$) at different activation times, compared to the baseline behavior (black line). The continuous red line shows the response for the case $T = 2(T_f/6)$, the dashed red line for $T = 3(T_f/6)$, and the blue line for $T = 4(T_f/6)$. For the same actuation location we observe either improvement or degradation of lift, depending on the activation phase.

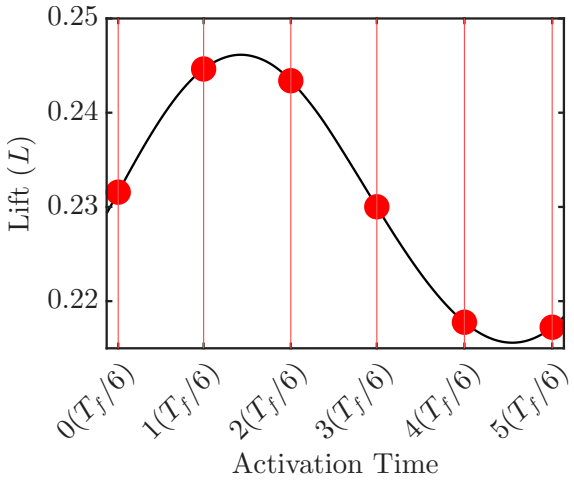

Fig. 9 Timing of the pulses in terms of the phase evolution of the baseline Lift signal.

C. Derivation of the Combined POD–CWT Scalogram Including Cross-Terms

While CWT of the lift coefficient provides a compact, case-wide time–frequency view, extending this analysis directly to the full velocity field is prohibitive: computing a scalogram at every spatial location is both computationally expensive and yields results that are difficult to compare across perturbation cases. To obtain a single, global time-frequency representation of the flow, we now employ the Convolutional Wavelet Transform (CWT) together with the Proper Orthogonal Decomposition (POD).

We first construct a common modal basis for all cases by applying snapshot-POD to a concatenated dataset of FTLE snapshots. Specifically, FTLE fields from 16 distinct actuation cases and one baseline case are stacked in time, and a single POD is performed on this aggregate dataset. The resulting POD spatial modes $\{\boldsymbol{\phi}_i(\mathbf{x})\}_{i=1}^{n}$ are shared across all cases, while each case has its own temporal coefficients $a_i(t)$ associated with a singular value σ_i.

To ensure that each mode's contribution is normalized, we define the *normalized* temporal coefficient

$$\widetilde{a}_i(t) \;=\; \frac{a_i(t)}{\sigma_i},$$

so that $\int_{-\infty}^{\infty} |\widetilde{a}_i(t)|^2 \, dt \;=\; 1$. This normalization casts each mode's dynamics on a common scale, facilitating direct

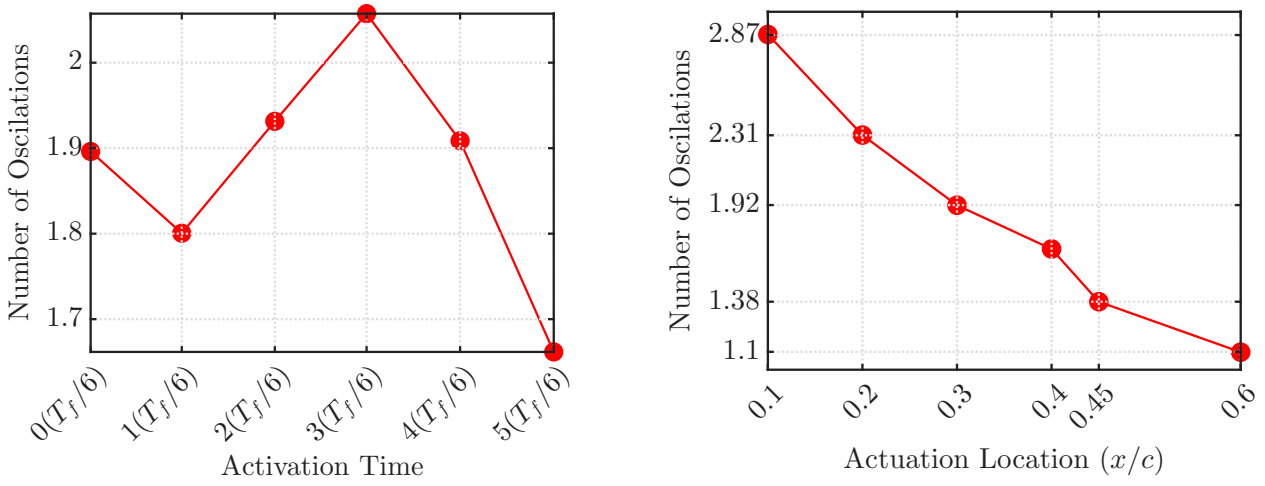

(a) Delay in the onset of transience (averaged over locations)

(b) Delay in the onset of transience (averaged over times)

Fig. 10 Number of baseline oscillations in the lift cycle after the actuation occurs and before transient energy growth begins. Figure (a) shows the average delay across all six location for a given pulse timing. Figure (b) shows the delay across all six pulsing times (for each location). Note that the bend between $x/c = 0.4$ and $x/c = 0.45$, corresponds to the separation point.

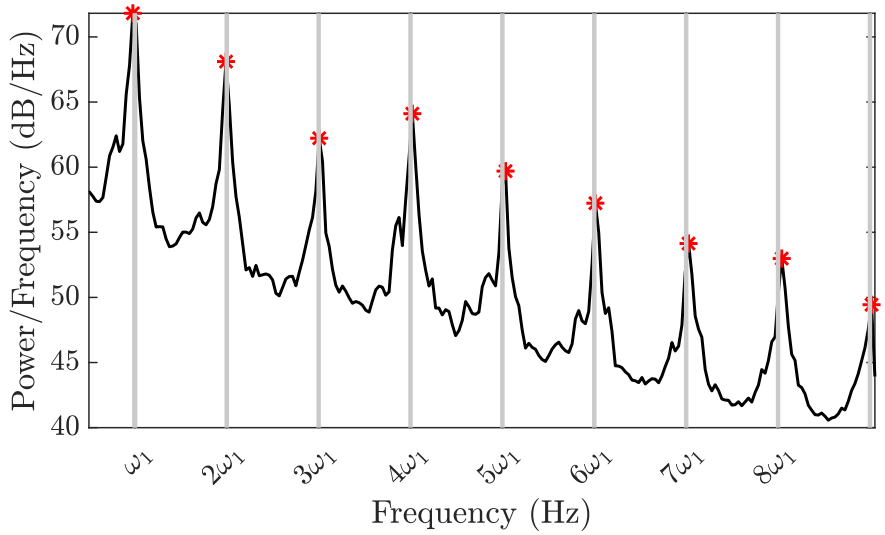

Fig. 11 Combined FFT of all POD Modes. Note the pronounced peaks at the harmonic frequencies (here, $\omega_1 = 2.76$).

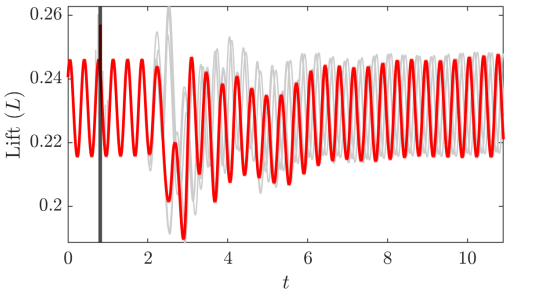

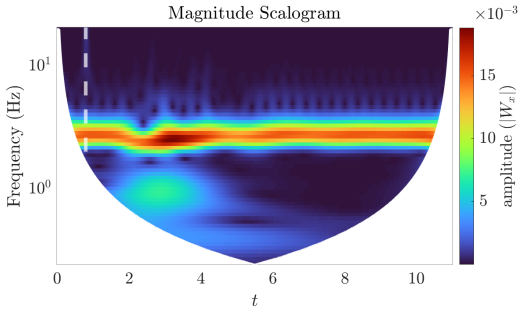

(a) $(x/c = 0.10)$ **for the case** $T = 2(T_f/6)$

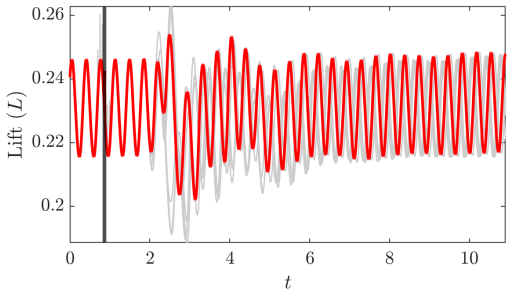

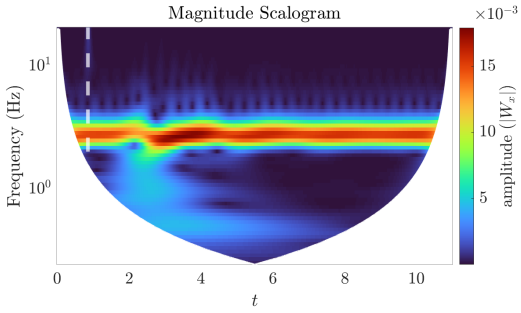

(b) $(x/c = 0.10)$ **for the case** $T = 3(T_f/6)$

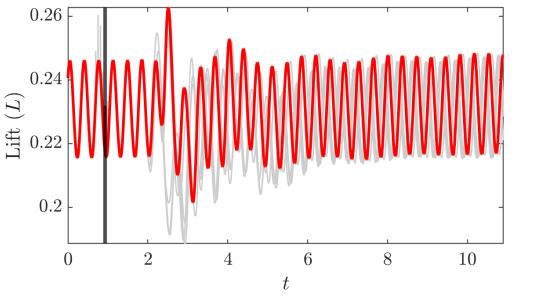

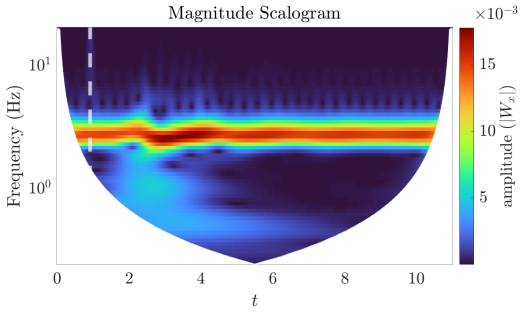

(c) $(x/c = 0.10)$ **for the case** $T = 4(T_f/6)$

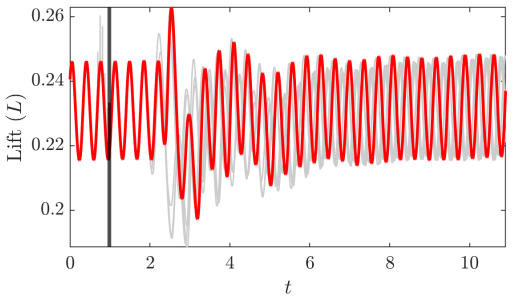

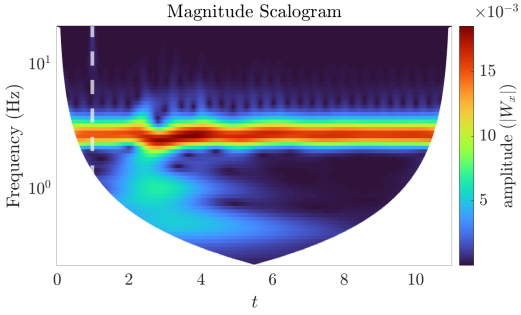

(d) $(x/c = 0.10)$ **for the case** $T = 5(T_f/6)$

Fig. 12 Lift responses and the corresponding magnitude scalograms for four temporal perturbation cases at $x/c = 0.1$**. The lift plots indicate the lift response as a red line, with the other lift responses plotted in gray for comparison. The Vertical lines in both the lift response and magnitude scalogram plots indicate the time at which the pulse occurs. Note that the Magnitude scalogram plots have a white cone of influence (shown as the white regions). This is due to the wavelet convolution resulting in smearing near the edges of the dataset.**

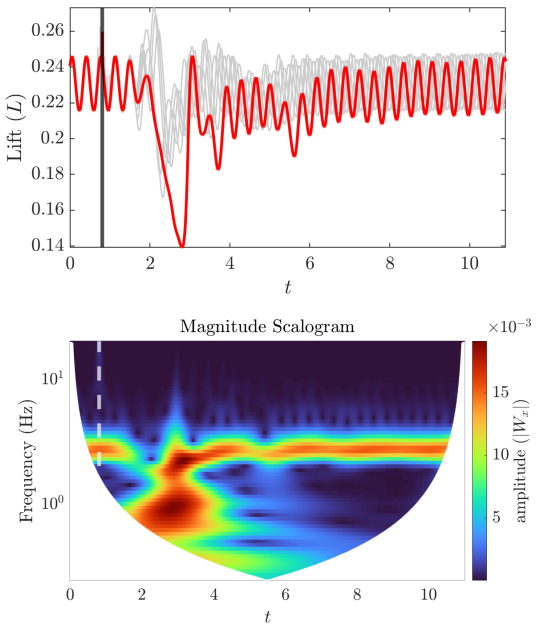

(a) $(x/c = 0.45)$ **for the case** $T = 2(T_f/6)$

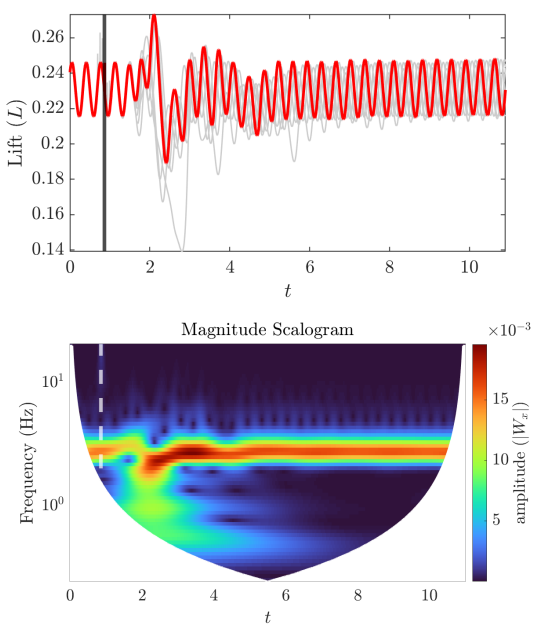

(b) $(x/c = 0.45)$ **for the case** $T = 3(T_f/6)$

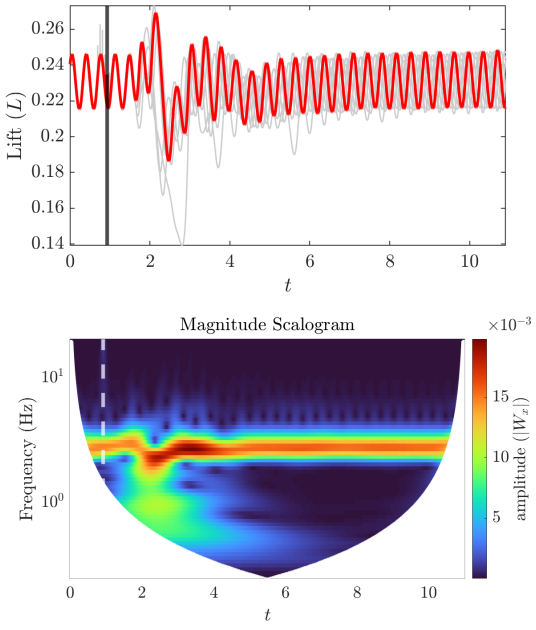

(c) $(x/c = 0.45)$ **for the case** $T = 4(T_f/6)$

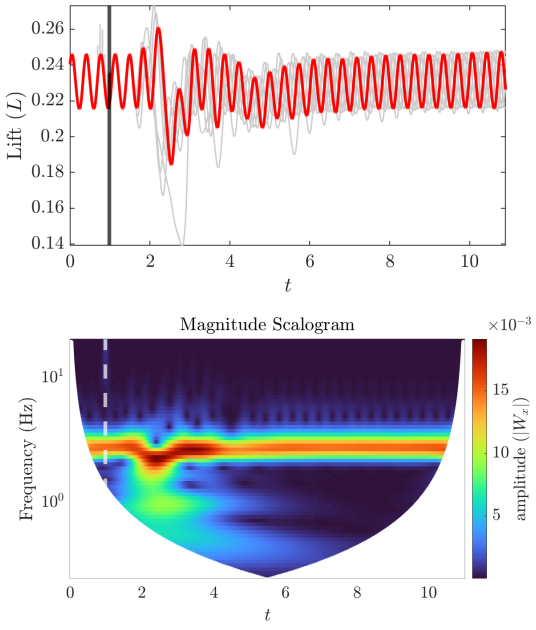

(d) $(x/c = 0.45)$ **for the case** $T = 5(T_f/6)$

Fig. 13 Lift responses and the corresponding magnitude scalograms for four temporal perturbation cases at $x/c = 0.45$. Note the significant decrease in lift for the case $T = 3(T_f/6)$, and the significant amplification of the lo-frequency bands.

comparison across modes. Next, we apply the CWT to each normalized coefficient $\widetilde{a}_i(t)$. Let $\psi_{s,\tau}(t)$ denote a dilated ($s > 0$) and translated (τ) mother wavelet of unit L^2 norm:

$$\psi_{s,\tau}(t) \;=\; \frac{1}{\sqrt{s}}\,\psi\Big(\tfrac{t-\tau}{s}\Big), \quad \int_{-\infty}^{\infty} |\psi_{s,\tau}(t)|^2\,dt = 1.$$

The CWT coefficient for mode i is then

$$W_i(s,\tau) = \int_{-\infty}^{\infty} \widetilde{a}_i(t)\,\overline{\psi_{s,\tau}(t)}\,dt,$$

which is a complex-valued function of scale s and time shift τ. To recover a global time–frequency representation of the original flow signal without truncation, we re-introduce each mode's singular value σ_i and sum across all n modes:

$$W_{\text{tot}}(s,\tau) = \sum_{i=1}^{n} \sigma_i\, W_i(s,\tau).$$

By construction, $W_{\text{tot}}(s,\tau)$ contains the complete modal contributions at each scale and time. The magnitude scalogram; i.e. the instantaneous power at each (s,τ) is defined as

$$P(s,\tau) = \big|W_{\text{tot}}(s,\tau)\big|^2 = \Big|\sum_{i=1}^{n} \sigma_i\, W_i(s,\tau)\Big|^2.$$

Expanding this square yields modal self-terms and cross-terms:

$$P(s,\tau) = \sum_{i=1}^{n} \sigma_i^2\,|W_i(s,\tau)|^2 \;+\; \sum_{\substack{i,j=1\\ i\neq j}}^{n} \sigma_i\,\sigma_j\,W_i(s,\tau)\,\overline{W_j(s,\tau)}.$$

Noting that the double sum over $i \neq j$ can be regrouped as twice the real part of $i < j$ interactions,

$$\sum_{i\neq j} \sigma_i\sigma_j\,W_i\overline{W_j} = 2\sum_{1\le i<j\le n} \sigma_i\,\sigma_j\,\Re\big\{W_i(s,\tau)\,\overline{W_j(s,\tau)}\big\}.$$

Thus, we arrive at the final expression:

$$P(s,\tau) = \underbrace{\sum_{i=1}^{n} \sigma_i^2\,|W_i(s,\tau)|^2}_{\text{(modal power sum)}} \;+\; \underbrace{2\sum_{1\le i<j\le n} \sigma_i\,\sigma_j\,\Re\big\{W_i(s,\tau)\,\overline{W_j(s,\tau)}\big\}}_{\text{(cross-term interactions)}}. \tag{7}$$

The first term aggregates each mode's individual energy contribution, while the second captures interactions between alternative modes, providing a comprehensive POD–CWT scalogram that includes all viable modal interactions.

Figure 14 shows spatial mode shapes extracted at the dominant harmonic and its first five overtones. These modes are obtained by first forming a POD basis of the FTLE field, $\mathbf{a}(\mathbf{x},t) \approx \sum_{j=1}^{r} a_j(t)\,\boldsymbol{\phi}_j(\mathbf{x})$, and then applying dynamic mode decomposition (DMD) to the temporal coefficients $a_j(t)$ [56, 57]. Let $\mathbf{A}$ denote the best-fit linear propagator that advances the POD state in time, $\mathbf{a}_{k+1} \approx \mathbf{A}\,\mathbf{a}_k$, obtained in a least-squares sense from consecutive snapshots. The eigendecomposition $\mathbf{A}\boldsymbol{\psi}_m = \lambda_m\boldsymbol{\psi}_m$ yields DMD eigenvalues $\lambda_m = \exp((\sigma_m + i\omega_m)\Delta t)$ and modes $\boldsymbol{\psi}_m$. Frequencies ω_m near integer multiples of the fundamental shedding frequency ω_1 are grouped, and the corresponding DMD modes are mapped back to physical space via the POD basis to obtain "frequency-wise" mode shapes associated with each harmonic band.

Panels (a)–(f) in Fig. 14 display the real part of the reconstructed FTLE mode shapes at $\omega_1 \approx 2.76$ and its first five harmonics. The dominant harmonic is concentrated along the separated shear layer and trailing-edge region, capturing the large-scale roll-up and global wake shedding. Higher harmonics exhibit progressively shorter streamwise wavelengths and finer structure within the shear layer: the second and third harmonics emphasize the breakdown of the primary rollers, while the fourth to sixth harmonics highlight small- scale filaments and secondary instabilities in the

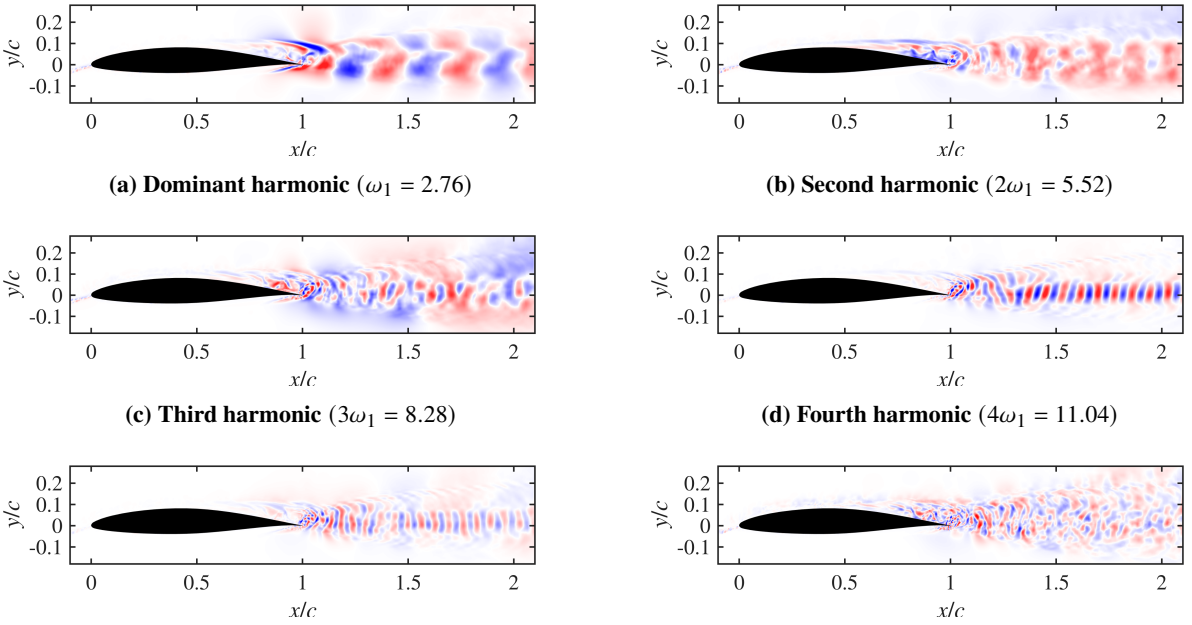

(a) Dominant harmonic ($\omega_1 = 2.76$)

(b) Second harmonic ($2\omega_1 = 5.52$)

(c) Third harmonic ($3\omega_1 = 8.28$)

(d) Fourth harmonic ($4\omega_1 = 11.04$)

(e) Fifth harmonic ($5\omega_1 = 13.80$)

(f) Sixth harmonic ($6\omega_1 = 16.56$)

Fig. 14 FTLE mode shapes obtained at the first six harmonics.

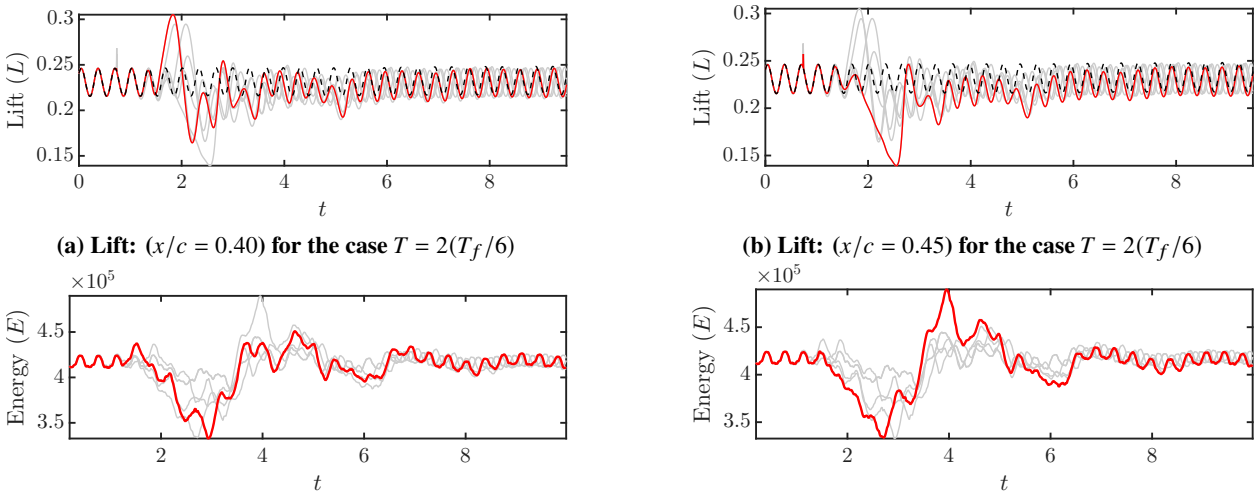

(a) Lift: ($x/c = 0.40$) **for the case** $T = 2(T_f/6)$

(b) Lift: ($x/c = 0.45$) **for the case** $T = 2(T_f/6)$

(c) Energy: ($x/c = 0.40$) **for the case** $T = 2(T_f/6)$

(d) Energy: ($x/c = 0.45$) **for the case** $T = 2(T_f/6)$

Fig. 15 Lift for the maximum lift and maximum drag case. Cumulative energy of all POD coefficients $a_i(t)$ for four different pulse timings at ($x/c = 0.45$).

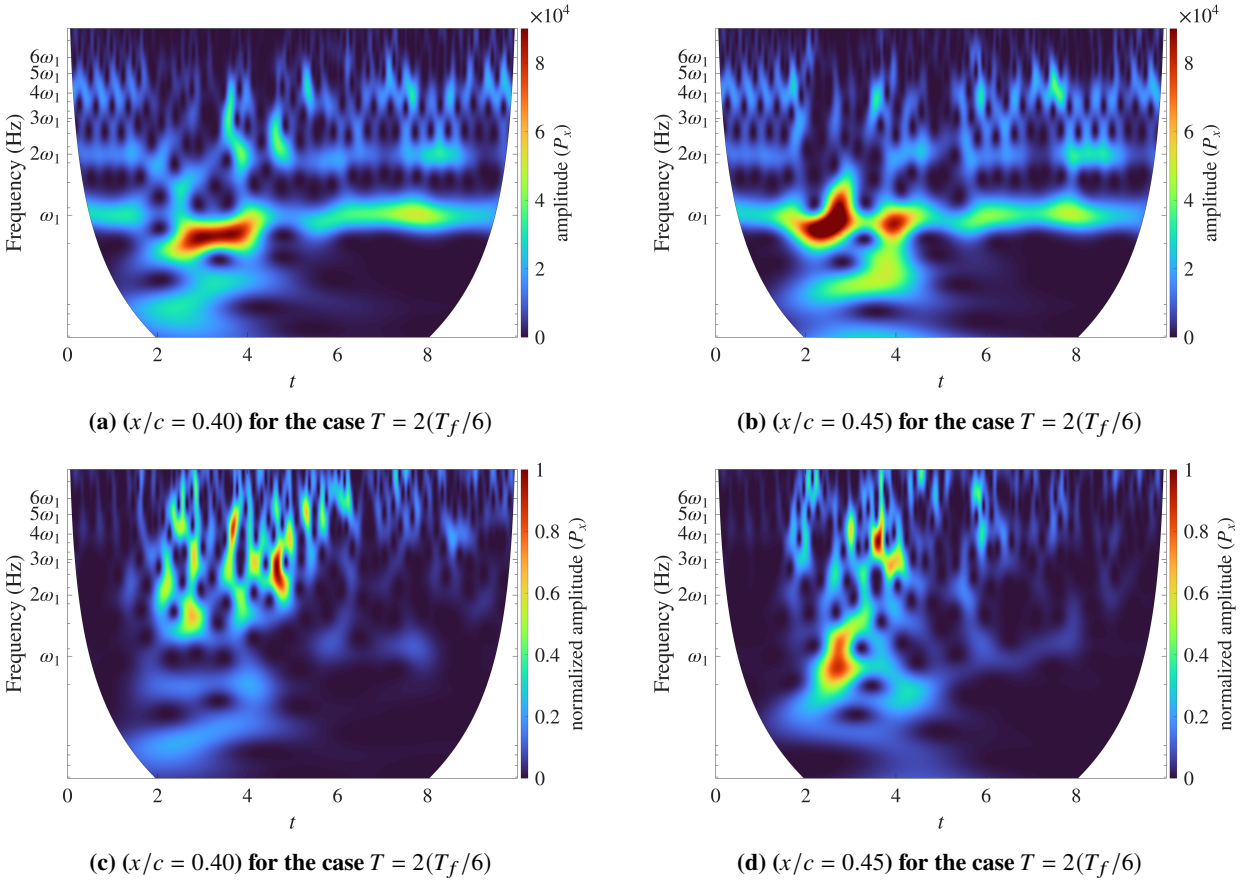

(a) $(x/c = 0.40)$ **for the case** $T = 2(T_f/6)$

(b) $(x/c = 0.45)$ **for the case** $T = 2(T_f/6)$

(c) $(x/c = 0.40)$ **for the case** $T = 2(T_f/6)$

(d) $(x/c = 0.45)$ **for the case** $T = 2(T_f/6)$

Fig. 16 Magnitude scalograms for max lift and max drag case. Plots (c) and (d) show the "flattened" POD scalograms. Note the significant amplification of the first harmonic band at ω_1 for the case at $x/c = 0.45$ case.

wake. Together, these frequency-conditioned modes provide a harmonic decomposition of the Lagrangian transport barriers, isolating how different scales of the Kelvin–Helmholtz cascade organize material separation and mixing.

Figure 11 summarizes the corresponding spectral content by plotting the power spectral density of the combined POD time coefficients. The spectrum exhibits pronounced peaks at ω_1, $2\omega_1$, …, $8\omega_1$, confirming that the FTLE dynamics are strongly organized by a nearly harmonic ladder of frequencies. The alignment between these peaks and the DMD-selected bands in Fig. 14 indicates that the extracted frequency-wise mode shapes capture the dominant oscillatory components of the Lagrangian flow structure.

Figure 15 first compares the temporal response of the flow for the "best" and "worst" pulsed cases, corresponding to $x/c = 0.40$ and $x/c = 0.45$ with $T = 2(T_f/6)$, respectively. Panels (a,b) show the lift coefficient $L(t)$ (red) overlaid with the baseline (dashed) and, in gray, the other pulse phases at the same location. At $x/c = 0.40$ the selected phase produces only a modest, quickly damped modulation of the lift about the baseline envelope. In contrast, the same phase at $x/c = 0.45$ generates a strong adverse transient: after a short delay the lift drops by roughly 35% before slowly recovering toward the baseline cycle. Panels (c,d) show the cumulative POD energy,

$$E(t) = \sum_{i=1}^{n} |a_i(t)|^2 = \|\mathbf{a}(t)\|_2^2,$$

where $a_i(t)$ are the POD temporal coefficients. The "good" case at $x/c = 0.40$ exhibits only a mild, short-lived dip in $E(t)$, whereas the $x/c = 0.45$ case shows a distinct energetic burst that is nonetheless small compared with the large baseline wake energy dominated by robust vortex shedding. This disparity between large force excursions and comparatively modest changes in $E(t)$ already hints at the extreme receptivity of the separated wake.

The hybrid POD–CWT scalograms in figures (a) and (b) of 16 provide a time–frequency view of this behavior. Starting from the POD expansion $\mathbf{q}(\mathbf{x}, t) \approx \sum_{i=1}^{n} a_i(t)\, \boldsymbol{\phi}_i(\mathbf{x})$, we compute the continuous wavelet transform of each temporal coefficient, $W_i(s, \tau) = \mathcal{W}[a_i](s, \tau)$, and then form a POD-weighted transform

$$W_{\text{tot}}(s, \tau) \;=\; \sum_{i=1}^{n} \sigma_i\, W_i(s, \tau),$$

where σ_i are the singular values associated with the modes. The resulting scalogram $P_a(s, \tau) = |W_{\text{tot}}(s, \tau)|$ for $x/c = 0.45$ (figure 16b) recovers the same dominant vortex-shedding band seen in the lift-based CWT (figure 13), but with far greater prominence relative to the broadband background. This amplification arises because the principal POD modes, which carry most of the wake energy, also possess the largest σ_i, so their wavelet coefficients $\sigma_i W_i$ dominate W_{tot}. In effect, the modes that encode the bulk of the flow energy appear more conspicuously in the scalogram, while weaker, higher-order dynamics are comparatively muted, consistent with the behaviour of the total energy $E(t)$ in figure 19.

Immediately after each perturbation pulse convects into the separation bubble, the POD–CWT scalograms exhibit a characteristic bifurcation: a brief burst of high-frequency energy, associated with small-scale shear-layer instabilities encoded in higher-order POD modes, is coupled with a simultaneous low-frequency response tied to the large-scale recirculating wake. The high-frequency bands indicate localized excitation of fine-scale structures in the separated shear layer, whereas the emergent low-frequency band reflects the growth and decay of separated wake vortices downstream. This dual-band signature validates the physical picture in which fine-scale structures respond first and then transfer energy into the broader wake, modulating the dominant shedding band near ω_1.

To identify which frequency bins are most directly amplified by the pulse, independent of mode energy, we also compute a "flat" scalogram by setting $\sigma_i = 1$ for all i, yielding $\widetilde{W}_{\text{tot}}(s, \tau) = \sum_i W_i(s, \tau)$ ((c) and (d) in figure 16). This unweighted transform highlights bursts of power concentrated in very high-frequency bands, appearing as intermittent, nearly discrete patches that suggest strong nonlinear interactions among modes. A few weaker low-frequency bands also persist, decaying slowly after the pulse and indicating residual large-scale modulation. We note that although the pulse at $x/c = 0.45$ with actuation at $T = 2(T_f/6)$ yields a pronounced drop in mean lift and increase in drag (figure 13), its global transient response measured by $\|\mathbf{a}(t)\|_2$ remains smaller than for other pulse timings that induce less dramatic changes in $L(t)$ (see figure 19). In the most energetic scenarios, pulses are timed to coincide with the wake's peak receptivity, injecting energy simultaneously into the dominant shedding band and multiple higher-order harmonics; the resulting broad-spectrum excitation fosters strong intermodal coupling and a nonlinear cascade, producing pronounced bursts across several frequency bands and elevating $\|\mathbf{a}(t)\|_2$. By contrast, other perturbations (e.g. at $x/c = 0.45$ and $T = 3(T_f/6)$) appear to primarily affect separation-region structures without effectively energizing the larger coherent

vortices downstream. Their scalograms show weaker coupling between bands and a more modest change in the norm. Together, these observations underscore the critical importance of phase-space alignment between perturbation timing, spatial location, and coherent-structure dynamics: only excitations that optimally engage both shear-layer instabilities and the global wake feedback yield the highest energy uptake and the richest multi-frequency response. Localised pulses thus trigger a strongly a strongly intermodal, yet highly selective, coupling in the separated flow.

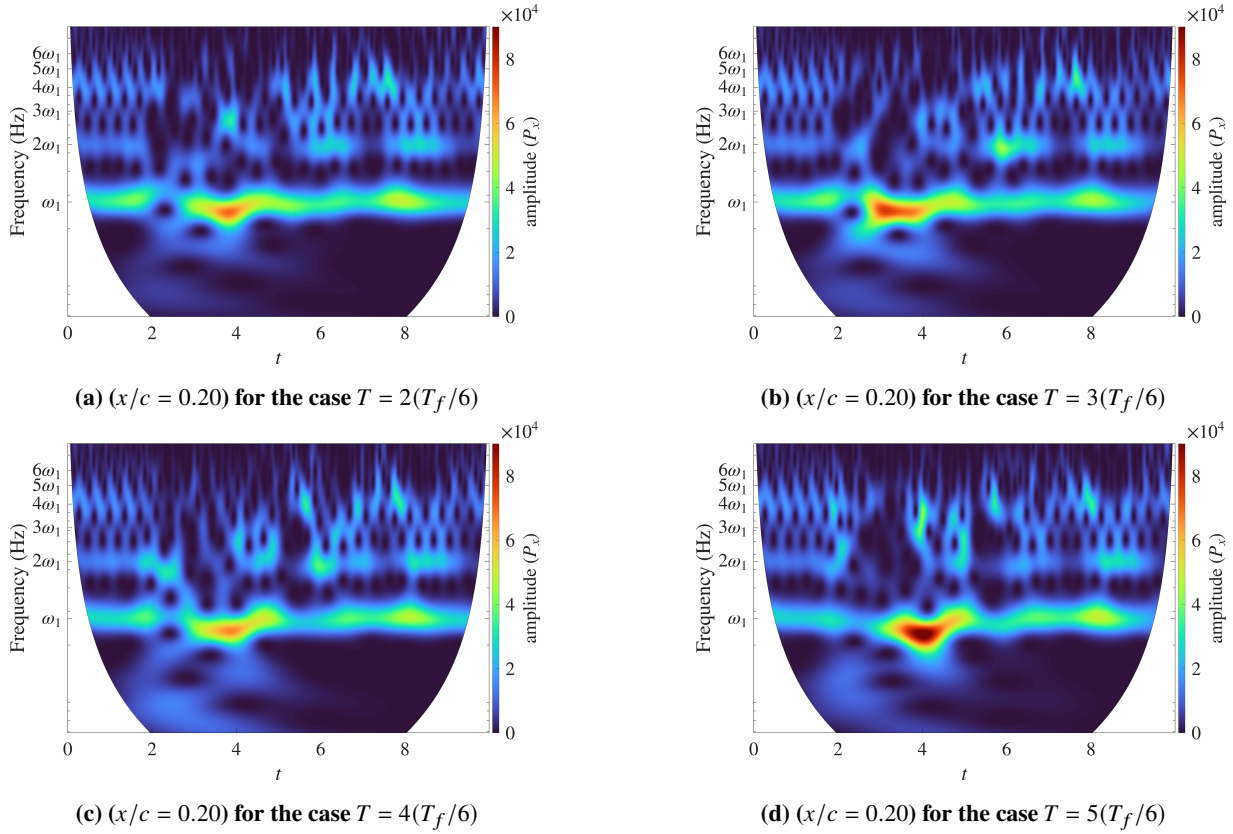

(a) $(x/c = 0.20)$ **for the case** $T = 2(T_f/6)$

(b) $(x/c = 0.20)$ **for the case** $T = 3(T_f/6)$

(c) $(x/c = 0.20)$ **for the case** $T = 4(T_f/6)$

(d) $(x/c = 0.20)$ **for the case** $T = 5(T_f/6)$

Fig. 17 Magnitude scalograms based on the aggregate contribution of the weighted POD modes for four different pulse timings at $x/c = 0.20$. Note the significant bifurcation that occurs some time after the perturbation reaches the separation bubble.

D. Lift, drag and Lagragian separation metrics

Figures 20 and 21 summarize the responses of lift, drag and Lagrangian separation metrics of the test matrix, formed by the Cartesian product of six pulsed actuation locations ($x/c \in \{0.10, 0.20, 0.30, 0.40, 0.45, 0.50\}$) and six pulsed activation times $\big(T \in \{0, (1/6)T_f, \ldots, 5(1/6)T_f\}$. Figure 20 reports, for each case, the extrema after actuation of lift and drag. The largest post-activation maximum lift and the smallest post-activation minimum drag occur for cases clustering around $x/c = 0.40$ with activation near $T = 2(T_f/6)$, and more generally over the alternating set $x/c \in \{0.20, 0.40, 0.50\}$. Conversely, combinations involving $x/c = 0.45$, particularly at $T = 2(T_f/6)$, exhibit markedly reduced minimum lift and elevated maximum drag, indicating a unfavorable change in the lift-to-drag relation.

To quantify aerodynamic performance more directly, figure 21 presents the post-activation maximum and time-averaged lift-over-drag ratio together with the maximum asymptotic separation and spiking angles. Cases with large *maximum* and *time-averaged* lift-over-drag and relatively mild increases in separation and spiking angles are concentrated near $x/c = 0.40$ with $T = 2(T_f/6)$, and within the broader group $x/c \in \{0.20, 0.40, 0.50\}$ (panels 21a,21b,21c,21d). In contrast, the combination $x/c = 0.45$, $T = 2(T_f/6)$ yields the lowest *time-averaged* lift-over-drag, the most pronounced drag penalty, and by far the largest maximum separation and spiking angles (panels 21b–21d), identifying it as the most detrimental configuration in the parametric set. The variation in the time-averaged lift-over-drag (values between 18 to 20), is substantially smaller than in the corresponding maxima (values between 21 and 28), indicating that the

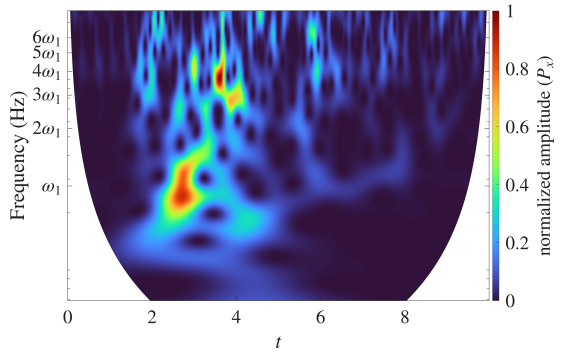

(a) $(x/c = 0.45)$ **for the case** $T = 2(T_f/6)$

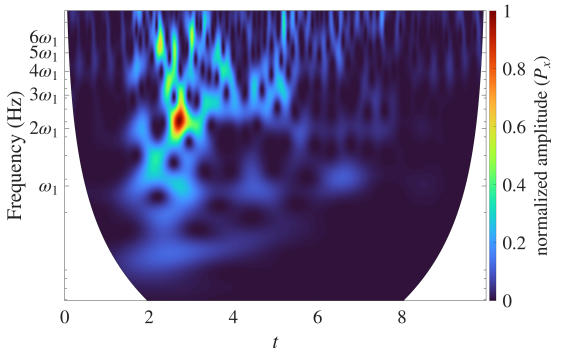

(b) $(x/c = 0.45)$ **for the case** $T = 3(T_f/6)$

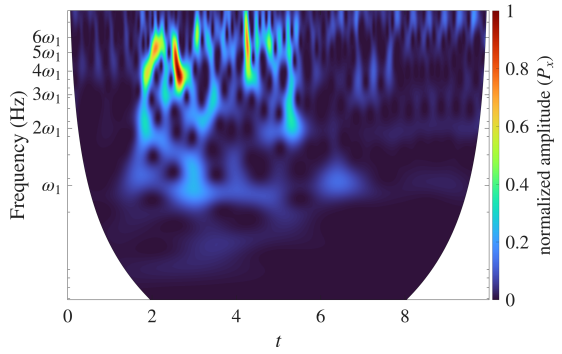

(c) $(x/c = 0.45)$ **for the case** $T = 4(T_f/6)$

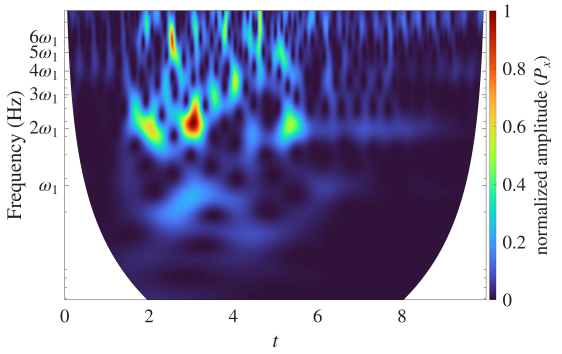

(d) $(x/c = 0.45)$ **for the case** $T = 5(T_f/6)$

Fig. 18 Magnitude scalograms based on the aggregate contribution of the normalized POD modes for four different pulse timings at $x/c = 0.45$. Here, each POD mode had an equal magnitude to show what frequency bands saw the greatest changes. Localized bursts indicate that modes are tightly coupled across frequencies, which is especially evident for the case $T = 2(T_f/6)$. We also note the significant amplification of the primary ban (ω_1) for this case. The duration of this amplification aligns with the the sharp drop in lift observed in figure 15.

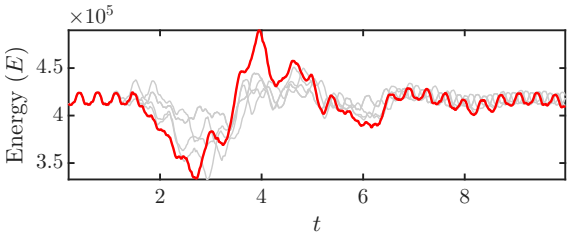

(a) $(x/c = 0.45)$ **for the case** $T = 2(T_f/6)$

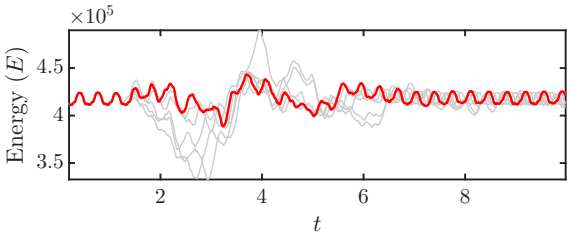

(b) $(x/c = 0.45)$ **for the case** $T = 3(T_f/6)$

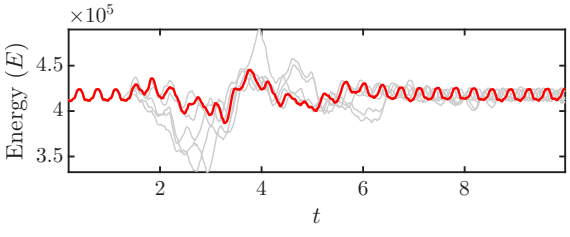

(c) $(x/c = 0.45)$ **for the case** $T = 4(T_f/6)$

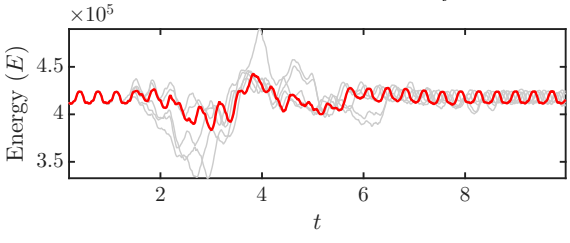

(d) $(x/c = 0.45)$ **for the case** $T = 5(T_f/6)$

Fig. 19 Global transient flow response $\|a(t)\|_2$ for four different pulse timings at $(x/c = 0.45)$.

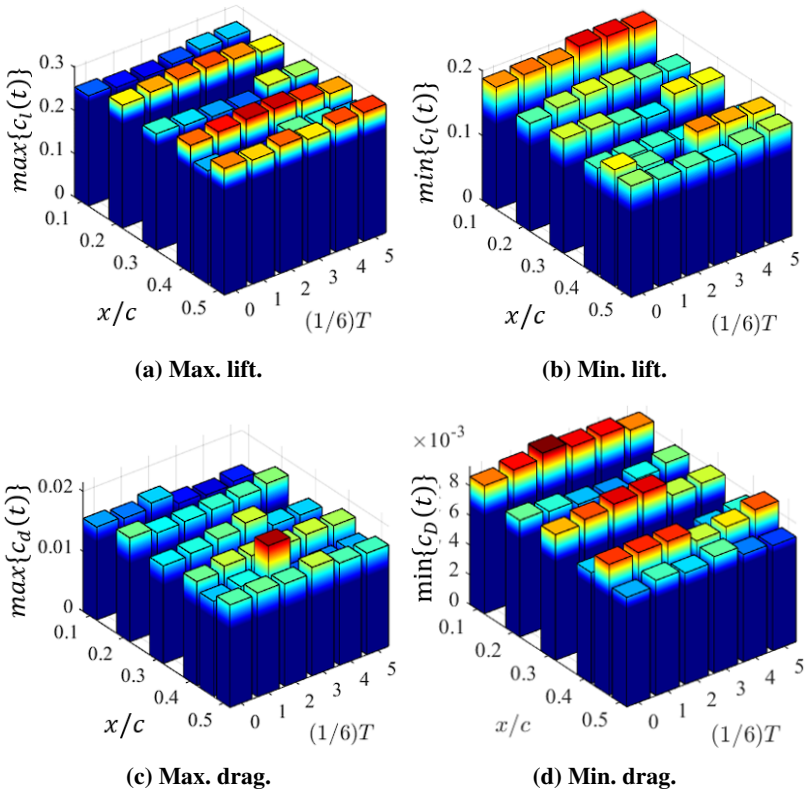

(a) Max. lift. **(b) Min. lift.**

(c) Max. drag. **(d) Min. drag.**

Fig. 20 Parametric study: post-activation extrema of lift and drag coefficients for the 36 pulsed cases. Each bar corresponds to one combination of actuation location and activation time.

instantaneous pulse predominantly alters the transient response while inducing only modest changes in the mean performance over the post-pulse interval.

Two robust trends emerge. *Phase sensitivity in time:* for a fixed location, the response flips as the activation time is shifted by approximately $T_f/2$; for example, at $x/c = 0.40$ the high maximum lift and lift-over-drag achieved at $T = 2(T_f/6)$ are mirrored by much smaller gains at $T = 5(T_f/6)$ (figures 20a,21a). This indicates that receptivity is locked to the shedding phase. *Spatial staggering in x/c:* adjacent actuation sites tend to alternate between favorable and unfavorable outcomes—roughly $\{0.10, 0.30, 0.45\}$ versus $\{0.20, 0.40, 0.50\}$—suggesting that the advective travel time from the pulse location to the trailing edge either aligns or detunes the K–H packet with the shedding cycle in a way that enhances or degrades aerodynamic efficiency. Additionally, (i) the case $x/c = 0.45$, $T = 2(T_f/6)$ is unusually sharp in both separation/spiking angles and drag, while neighboring settings are much milder; a small $0.05c$ upstream shift (to $x/c = 0.40$) at the same time window switches the outcome from strongly degrading to strongly favorable; and (ii) upstream actuation at $x/c = 0.20$ can still be beneficial when timed near $2(T_f/6)$, but its gains in lift-over-drag are generally smaller than those at $x/c = 0.40$, consistent with weaker coupling to the separated shear layer. These observations support the hypothesis that locations around the spiking manifold are optimal for producing substantial, yet efficient, modifications of the aerodynamic response. Taken together, the parametric trends emphasize that optimal outcomes require *coordinating* both the streamwise placement and the activation phase so that the convecting K–H packet reaches the trailing edge in a phase that enhances lift while limiting drag.

IV. Conclusions

A parametric time–frequency study is conducted on the pulsed actuation control of a separated flow, with low-Reynolds-number, and over a cambered NACA 65(1)-412 airfoil at $Re_c = 20{,}000$, $M = 0.3$ and $\alpha = 4°$. Short, zero-net-mass-flux Gaussian pulses were introduced at selected chordwise locations and phases of the natural shedding cycle, and their impact on the separated shear layer and wake was quantified using a combination of Lagrangian

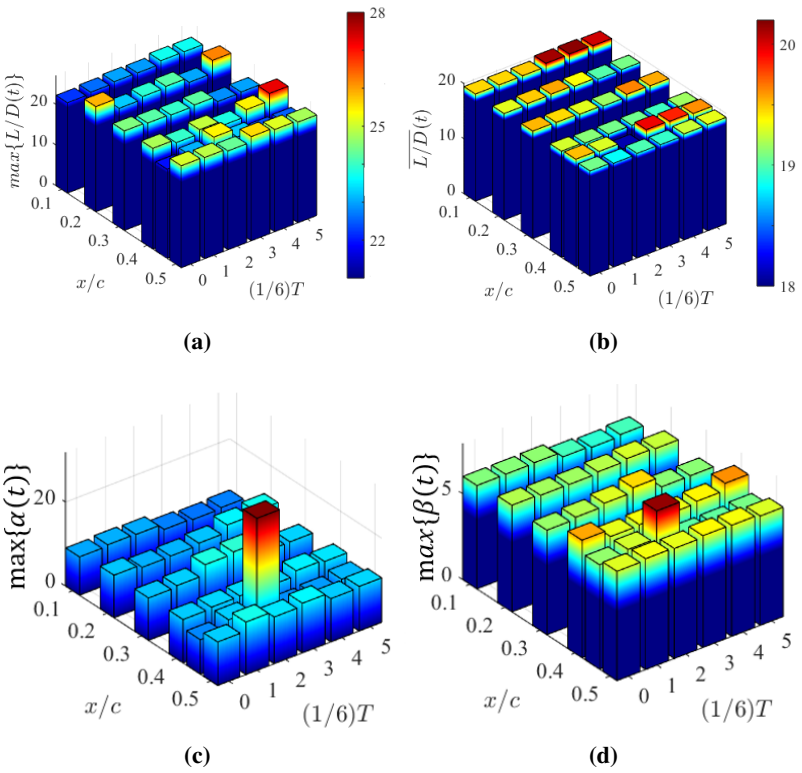

Fig. 21 Parametric study: post-activation (a) maximum and (b) time average of lift-over-drag ratio, L/D and (c) maximum instantaneous asymptotic separation angles, $\alpha(t)$ and (d) spiking angles (d), $\beta(t)$.

diagnostics (FTLE, separation and spiking angles) and time–frequency analysis (CWT and POD–CWT).

Brief, phase-locked pulses placed near Lagrangian spiking separation locations point towards an optimal placement of actuators upstream of asymptotic separation manifolds and close to spiking backbones. The optimal actuation is also influenced by several, non-trivial temporal scales. Pulses placed near the origin of the so-called backbone of separation ($x/c \approx 0.4$) and triggered at a specific phase produced the greatest increase in the time-averaged lift over drag ratio. A marginal downstream shift of the pulse to $x/c = 0.45$ at the same phase produces the opposite effect, with up to $O(30\%)$ lift loss and a substantial drag penalty. For a fixed location, shifting the actuation by approximately half a shedding period reverses the sign of the response. Either way, the region upstream of the asymptotic separation manifold was shown to be the most receptive to instantaneous perturbations for the greatest changes on output aerodynamic forces.

Forward and backward FTLE fields provide insights into the Kelvin-Helmholtz instability and the interlocking mechanism. The K-H instability opens gaps in ridges in the forward FTLE field coinciding with the separation shear-layer. These gaps enhance entrainment into the separated region. Here, the K-H instability is amplified with the gap and its wavelength increasing as the K-H packet advects towards the trailing edge at which point it combines with the Lagrangian flow structure at the trailing edge into an interlocking material surface. Depending on its phase and position relative to the trailing edge, this surface either traps an adverse vortex near the suction side, causing a pronounced lift drop, or promotes transient reattachment and yields up to $O(30\%)$ lift enhancement. Thus, the optimallity of actuation is encoded in the spatio–temporal evolution of this interlocking surface.

The combined POD–CWT framework provides a compact, global representation of the pulsed response. By constructing a common POD basis from all pulsed cases and applying the continuous wavelet transform to the energy-normalized temporal coefficients, we obtain mode-wise scalograms that can be recombined into a single, case-comparable time–frequency map of the flow. This POD–CWT scalogram isolates the frequency band associated with the shear-layer K–H instability and identifies narrow windows of maximal energy injection tied to specific actuation phases and locations. In this way, it bridges global force measurements, local velocity probes, and Lagrangian structure, offering a practical diagnostic tool for future reduced-order modeling and controller design.

Future work will extend this framework to three-dimensional configurations, multi-pulse or periodic actuation, and

closed-loop control schemes in which the separation and spiking angles, or their surrogates, are used directly as feedback variables.

Acknowledgments

We gratefully acknowledge funding by the Air Force Office of Scientific Research under FA9550-21-1-0434.

References

[1] Gad-el-Hak, M., *Flow Control: Passive, Active, and Reactive Flow Management*, Cambridge University Press, Cambridge, United Kingdom, 2000.

[2] Williams, D. R., and MacMynowski, D. G., "Brief history of flow control," *Fundamentals and Applications of Modern Flow Control*, edited by R. D. Joslin and D. N. Miller, American Institute of Aeronautics and Astronautics, Reston, VA, 2009, Chap. 1, pp. 1–20.

[3] Schlichting, H., and Gersten, K., *Boundary-Layer Theory*, Springer-Verlag, New York, 1999.

[4] Cattafesta, L. N., and Sheplak, M., "Actuators for active flow control," *Ann. Rev. Fluid Mech.*, Vol. 43, 2011, pp. 247–272.

[5] Sosa, R., Artana, G., Moreau, E., and Touchard, G., "Stall control at high angle of attack with plasma sheet actuators," *Experiments in fluids*, Vol. 42, No. 1, 2007, pp. 143–167.

[6] Little, J., and Samimy, M., "High-lift airfoil separation with dielectric barrier discharge plasma actuation," *AIAA journal*, Vol. 48, No. 12, 2010, pp. 2884–2898.

[7] Mabe, J., Calkins, F., Wesley, B., Woszidlo, R., Taubert, L., and Wygnanski, I., "Single dielectric barrier discharge plasma actuators for improved airfoil performance," *Journal of Aircraft*, Vol. 46, No. 3, 2009.

[8] Cerretelli, C., and Kirtley, K., "Boundary Layer Separation Control with Fluidic Oscillators," *Journal of Turbomachinery*, Vol. 131, No. 4, 2009.

[9] Gregory, J., and Tomac, M. N., "A Review of Fluidic Oscillator Development," *AIAA Paper 2013-2474*, 2013.

[10] Woszidlo, R., and Wygnanski, I., "Parameters Governing Separation Control with Sweeping Jet Actuators," *AIAA Paper 2011-3172*, 2011.

[11] Seo, J. H., Cadieux, F., Mittal, R., Deem, E., and Cattafesta, L., "Effect of synthetic jet modulation schemes on the reduction of a laminar separation bubble," *Phys. Rev. Fluids*, Vol. 3, No. 3, 2018.

[12] Ostermann, F., Woszidlo, R., Nayeri, C. N., and Paschereit, C. O., "The Interaction Between a Spatially Oscillating Jet Emitted by a Fluidic Oscillator and a Crossflow," *Journal of Fluid Mechanics*, 2018.

[13] Amitay, M., Smith, B., and Glezer, A., "Aerodynamic flow control using synthetic jet technology," *36th AIAA Aerospace Sciences Meeting and Exhibit*, 1998.

[14] Amitay, M., Smith, D. R., Kibens, V., Parekh, D. E., and Glezer, A., "Aerodynamic Flow Control over an Unconventional Airfoil Using Synthetic Jet Actuators," *AIAA Journal*, Vol. 39, No. 3, 2001.

[15] Glezer, A., and Amitay, M., "Synthetic Jets," *Annual Review of Fluid Mechanics*, Vol. 34, No. 1, 2002, pp. 503–529.

[16] Amitay, M., Smith, B., and Glezer, A., "Aerodynamic flow control using synthetic jet technology," *36th AIAA Aerospace Sciences Meeting and Exhibit*, 1998.

[17] Glezer, A., and Amitay, M., "Synthetic jets," *Annual review of fluid mechanics*, Vol. 34, No. 1, 2002, pp. 503–529.

[18] Hemati, M., Deem, E., Williams, M., Rowley, C. W., and Cattafesta, L. N., "Improving separation control with noise-robust variants of dynamic mode decomposition," *54th AIAA Aerospace Sciences Meeting*, 2016, p. 1103.

[19] Deem, E., Cattafesta, L., Yao, H., Hemati, M., Zhang, H., and Rowley, C., "Experimental Implementation of Modal Approaches for Autonomous Reattachment of Separated Flows," *AIAA Aerospace Sciences Meeting*, 2018, pp. AIAA Paper 2018–1052.

[20] Seo, J., Cadieux, F., Mittal, R., Deem, E., and Cattafesta, L., "Effect of synthetic jet modulation schemes on the reduction of a laminar separation bubble," *Physical Review Fluids*, Vol. 3, No. 033901, 2018.

[21] Deem, E., Cattafesta, L., Hemati, M., Zhang, H., Rowley, C., and Mittal, R., "Adaptive Separation Control of a Laminar Boundary Layer using Online Dynamic Mode Decomposition," , 2020.

[22] Prandtl, L., "Uber Flussigkeitsbewegung bei sehr kleiner Reibung." *Verh. III, Int. Math. Kongr.*, Heidelberg, 1904.

[23] ROTT, N., "UNSTEADY VISCOUS FLOW IN THE VICINITY OF A STAGNATION POINT," *Quarterly of Applied Mathematics*, Vol. 13, No. 4, 1956, pp. 444–451. URL http://www.jstor.org/stable/43634278.

[24] Moore, F. K., *On the separation of the unsteady laminar boundary layer*, Springer Berlin Heidelberg, Berlin, Heidelberg, 1958, pp. 296–311. https://doi.org/10.1007/978-3-642-45885-9_23, URL https://doi.org/10.1007/978-3-642-45885-9_23.

[25] Sears, W. R., and Telionis, D. P., "Boundary-Layer Separation in Unsteady Flow," *SIAM Journal on Applied Mathematics*, Vol. 28, No. 1, 1975, pp. 215–235. URL http://www.jstor.org/stable/2100473.

[26] Liu, C. S., and Wan, Y.-H., "A Simple Exact Solution of the Prandtl Boundary Layer Equations Containing a Point of Separation," *Archive for Rational Mechanics and Analysis*, 1985. https://doi.org/10.1007/BF00282331, URL https://doi.org/10.1007/BF00282331.

[27] Sychev, V. V., Ruban, A. I., Sychev, V. V., and Korolev, G. L., *Asymptotic Theory of Separated Flows*, Cambridge University Press, 1998.

[28] Shariff, K., Pulliam, T., and Ottino, J., "A dynamical systems analysis of kinematics in the time-periodic wake of a circular cylinder," *Lectures in Applied Mathematics*, Vol. 28, 1991, pp. 613–646. URL https://ntrs.nasa.gov/citations/19930073989.

[29] Yuster, T., and Hackborn, W. W., "On invariant manifolds attached to oscillating boundaries in Stokes flows," *Chaos*, Vol. 7, No. 4, 1997, pp. 769–776.

[30] Haller, G., "Exact theory of unsteady separation for two-dimensional flows," *Journal of Fluid Mechanics*, Vol. 512, 2004, p. 257–311.

[31] Serra, M., Vetel, J., and Haller, G., "Exact theory of material spike formation in flow separation," *Journal of Fluids Mechanics*, Vol. 845, 2018, pp. 51–92.

[32] Yarusevych, S., Kawall, J., and Sullivan, P. E., "Airfoil performance at low Reynolds numbers in the presence of periodic disturbances," *Journal of fluids engineering*, Vol. 128, No. 3, 2006.

[33] Postl, D., Balzer, W., and Fasel, H., "Control of laminar separation using pulsed vortex generator jets: Direct numerical simulations," *Journal of Fluid Mechanics*, Vol. 676, 2011.

[34] Marxen, O., Kotapati, R., Mittal, R., and Zaki, T., "Stability analysis of separated flows subject to control by zero-net-mass-flux jet," *Physics of Fluids*, Vol. 27, No. 2, 2015.

[35] Yarusevych, S., and Kotsonis, M., "Steady and transient response of a laminar separation bubble to controlled disturbances," *Journal of Fluid Mechanics*, Vol. 813, 2017.

[36] Raju, R., Mittal, R., and Cattafesta, L., "Dynamics of airfoil separation control using zero-net mass-flux forcing," *AIAA Journal*, Vol. 46, No. 12, 2008.

[37] Mittal, R., and Kotapati, R. B., "Resonant mode interaction in a canonical separated flow," *IUTAM Symposium on Laminar-Turbulent Transition*, Springer, 2006, pp. 341–348.

[38] Mittal, R., Kotapati, R., and Cattafesta, L., "Numerical study of resonant interactions and flow control in a canonical separated flow," *43rd AIAA Aerospace Sciences Meeting and Exhibit, AIAA 2005-1261*, 2005.

[39] Yeh, C.-A., and Taira, K., "Resolvent-analysis-based design of airfoil separation control," *Journal of Fluid Mechanics*, Vol. 867, 2019, pp. 572–610.

[40] Taira, K., Hemati, M. S., Brunton, S. L., Sun, Y., Duraisamy, K., Bagheri, S., Dawson, S. T. M., and Yeh, C.-A., "Modal Analysis of Fluid Flows: Applications and Outlook," , 2019. ArXiv:1903.05750.

[41] Deem, E. A., Cattafesta, L., Zhang, H., Rowley, C., Hemati, M., Cadieux, F., and Mittal, R., "Identifying dynamic modes of separated flow subject to ZNMF-based control from surface pressure measurements," AIAA Paper 2017-3309, American Institute of Aeronautics and Astronautics, 2017.

[42] Hemati, M. S., Rowley, C. W., Deem, E. A., and Cattafesta, L. N., "De-biasing the dynamic mode decomposition for applied Koopman spectral analysis of noisy datasets," *Theoretical and Computational Fluid Dynamics*, Vol. 31, No. 4, 2017, pp. 349–368.

[43] Kamphuis, M., Jacobs, G. B., Chen, K., Spedding, G., and Hoeijmakers, H., *Pulse Actuation and Its Effects on Separated Lagrangian Coherent Structures for Flow over aCambered Airfoil*, 2018. https://doi.org/10.2514/6.2018-2255, URL https://arc.aiaa.org/doi/abs/10.2514/6.2018-2255.

[44] Bhattacharjee, D., Hemati, M., Klose, B., and Jacobs, G., *Optimal Actuator Selection for Airfoil Separation Control*, 2018. https://doi.org/10.2514/6.2018-3692, URL https://arc.aiaa.org/doi/abs/10.2514/6.2018-3692.

[45] Nelson, D. A., Jacobs, G. B., and Kopriva, D. A., "Effect of Boundary Representation on Viscous, Separated Flows in a Discontinuous-Galerkin Navier-Stokes Solver," *Theoretical Computational Fluid Dynamics*, Vol. 30, 2016, pp. 363–385.

[46] Klose, B. F., Jacobs, G. B., and Serra, M., "Kinematics of Lagrangian flow separation in external aerodynamics," *AIAA Journal*, Vol. 58, 2020, pp. 1926–1938. https://doi.org/10.2514/1.J059026.

[47] Klose, B. F., Spedding, G. R., and Jacobs, G. B., "Flow separation, instability and transition to turbulence on a cambered airfoil at Reynolds number 20 000," *Journal of Fluid Mechanics*, Vol. 1009, 2025, p. A9. https://doi.org/10.1017/jfm.2025.212.

[48] Torrence, C., and Compo, G. P., "A Practical Guide to Wavelet Analysis," *Bulletin of the American Meteorological Society*, Vol. 79, No. 1, 1998, pp. 61–78.

[49] Farge, M., "Wavelet Transforms and Their Applications to Turbulence," *Annual Review of Fluid Mechanics*, Vol. 24, 1992, pp. 395–458.

[50] Klose, B. F., Jacobs, G. B., and Kopriva, D. A., *On the robustness and accuracy of marginally resolved discontinuous Galerkin schemes for two dimensional Navier-Stokes flows*, 2019. https://doi.org/10.2514/6.2019-0780, URL https://arc.aiaa.org/doi/abs/10.2514/6.2019-0780.

[51] Jacobs, G., Kopriva, D., and Mashayek, F., *Outflow boundary conditions for the multidomain staggered-grid spectral method for the Navier-Stokes equations*, 2002. https://doi.org/10.2514/6.2002-903, URL https://arc.aiaa.org/doi/abs/10.2514/6.2002-903.

[52] Nelson, D. A., and Jacobs, G. B., "DG-FTLE: Lagrangian Coherent Structures with High-Order Discontinuous-Galerkin Methods," *Journal of Computational Physics*, Vol. 295, 2015, pp. 65–86.

[53] Suzuki, T., Colonius, T., and Pirozzoli, S., "Vortex shedding in a two-dimensional diffuser: theory and simulation of separation control by periodic mass injection," *Journal of Fluid Mechanics*, Vol. 520, 2004, pp. 187–213.

[54] Armstrong, K., "How does inertial particle dispersion relate to the finite time Lyapunov exponent in a vortex dominated wake?" Master's thesis, San Diego State University, 2008.

[55] Klose, B., Serra, M., and Jacobs, G., "Objective early identification of kinematic instabilities in shear flows," *arXiv preprint arXiv:2009.05851*, 2020. Submitted to Journal of Fluid Mechanics.

[56] Schmid, P. J., "Dynamic mode decomposition of numerical and experimental data," *Journal of Fluid Mechanics*, Vol. 656, 2010, pp. 5–28.

[57] Rowley, C. W., Mezić, I., Bagheri, S., Schlatter, P., and Henningson, D. S., "Spectral analysis of nonlinear flows," *Journal of Fluid Mechanics*, Vol. 641, 2009, pp. 115–127.